Title
Effect of Nanoporosity on the Thermal Conductivity of Amorphous Carbon

Author
Fujii, Amanda

Publication Date
2014

Peer reviewed|Thesis/dissertation

UNIVERSITY OF CALIFORNIA

Los Angeles

Effect of Nanoporosity on the Thermal Conductivity of Amorphous Carbon

A thesis submitted in partial satisfaction
of the requirements for the degree Master of Science
in Mechanical Engineering

by

Amanda Mei Keiko Fujii

2014

ABSTRACT OF THE THESIS

Effect of Nanoporosity
on the Thermal Conductivity of Amorphous Carbon

by

Amanda Mei Keiko Fujii

Master of Science in Mechanical Engineering
University of California, Los Angeles, 2014
Professor Laurent Pilon, Chair

The thermal conductivity of nanoporous amorphous carbon at 300 K was predicted using equilibrium molecular dynamics simulations based on the Green-Kubo method. The adaptive intermolecular reactive empirical bond order (AIREBO) potential was used to model carbon-carbon atomic interactions. Nanoporous amorphous carbon was simulated by removing a spherical region of atoms from the amorphous carbon matrix. Pore diameter varied between 9.76 and 26.0 Å and porosity ranged from 5 to 40%. The predicted effective thermal conductivity of nanoporous amorphous carbon was in good agreement with the Maxwell Garnett effective medium approximation (EMA) for porosity between 0 and 40%. Furthermore, the effective thermal conductivity was found to be proportional to $\rho_{eff}^{1.2}$ where ρ_{eff} is the effective density.

The thesis of Amanda Mei Keiko Fujii is approved

Adrienne Lavine

Jeff Eldredge

Laurent Pilon, Committee Chair

University of California, Los Angeles

2014

Contents

List of Figures

List of Tables

NOMENCLATURE

a_{ij}	limits the interaction with the first neighbor shell in the Tersoff potential
b_{ij}	measure of bond order in the Tersoff potential
d_p	pore diameter [Å]
dr	thickness of spherical shell
E	intermolecular potential
E_2	pair potential in the EDIP potential
E_3	three-body potential in the EDIP potential
f	frequency [THz]
f_c	smoothing cutoff function in the Tersoff potential
f_v	porosity
$g(r)$	radial distribution function
$G(r)$	reduced radial distribution function
$\hbar$	Planck's constant divided by 2π, $\hbar = 1.05 \times 10^{-34}$ J·s
$J(t)$	heat current [J·m/s]
$\langle J(0)J(t)\rangle$	heat current autocorrelation function
k	thermal conductivity [W/m·K]
k_B	Boltzmann constant, $k_B = 1.38 \times 10^{-23}$ J/K
k_c	thermal conductivity of the continuous phase [W/m·K]
k_d	thermal conductivity of the dispersed phase [W/m·K]
Kn	Knudsen number
ℓ	mean free path of gas inside pores [m]
L	system length (Å)
M	Molar mass [g/mol]
$n(r)$	average number of atoms in a spherical shell of thickness dr
n_0	number density of atoms [#/m^3]
N_A	Avogadro's constant, $N_A = 6.022 \times 10^{23}$ at/mol

$\langle n \rangle$	average coordination number
p	pressure [Pa]
r	distance of spherical shell from reference particle [m]
r_{ij}	distance between atoms i and j
t_{max}	total simulation time (ns)
T	temperature [K]
T_p	pyrolysis temperature [°C]
v_ℓ	longitudinal velocity of sound mode [m/s]
v_t	transverse velocity of sound mode [m/s]
V	volume [m^3]
Y	Young's modulus [Pa]
Z_i	effective coordination number of atom i

Symbols

β	coefficient in Equation (10)
θ_{jik}	angle between atom j and atom k subtended at atom i [rad]
Θ_i	cutoff temperature of phonon mode i [K]
ρ	density [g/cm^3]
σ	diameter of gas molecules represented by hard spheres [m]
τ	correlation time [ps]
$\Delta\tau_{max}$	maximum correlation time averaging window [ps]
ν	Poisson's ratio
Δt	time step (fs)

Subscripts

A	refers to the attractive contribution in the Tersoff potential
c	refers to the continuous phase
d	refers to the dispersed phase
$d, 0$	refers to the bulk property of the dispersed phase
eff	refers to the effective property

i	refers to polarization (2 transverse and 1 longitudinal)
LJ	refers to the Lennard-Jones intermolecular interactions
R	refers to the repulsive contribution in the Tersoff potential
$REBO$	refers to the REBO potential
$tors$	refers to torsional intermolecular interactions

ACKNOWLEDGEMENTS

First, I would like to extend my deepest thanks to Professor Laurent Pilon for his advice, motivation, and instruction. I initially wanted him as a graduate advisor because I knew he would challenge me academically. He has helped me grow both professionally and personally beyond what I could have expected. Through his guidance I have achieved the confidence and direction that I was lacking before starting my graduate degree. For these and much more I am deeply grateful. Additionally, I would like to thank Professor Adrienne Lavine and Professor Jeff Eldredge for their challenging and stimulating coursework and for serving on my thesis committee.

I would also like to thank my lab members for their knowledge and friendship. In particular, to Jin Fang for allowing me to consult him even after he had graduated. The time he spent introducing me to the theory and software programs that I applied to my research were invaluable as I began my graduate work. I would also like to thank Zander Thiele for his humor and optimism that kept me motivated in the lab. I wish him the best of luck as he continues his graduate work.

Furthermore, I am grateful for the officers in UCLA's Tau Beta Pi chapter who have allowed me to act as alumna advisor for the past two years. It has been a joy to watch the organization evolve, and I appreciate the opportunities Tau Beta Pi has provided me to keep me involved in the UCLA community. I am also grateful for the many friendships that I have developed through my association with Tau Beta Pi. A special thanks to Bryan Ngo for writing a script for me that helped my data processing run much faster.

Finally, I would like to thank my friends and family for their continual support. I am incredibly grateful for Rachel Older, Andrew Lewis, and Tom Kinzinger, my home away from home. As always, thank you to my parents and sister for their love and encouragement during my graduate studies and throughout my life. Lastly, thank you to Hunter Jones for his support during the home stretch.

1 Introduction

Electric double layer capacitors (EDLCs) store energy in electric double layer forming at the electrode-electrolyte interface by reversible ion adsorption [17]. Unlike typical electrical energy storage devices, such as batteries or dielectric capacitors, EDLCs exhibit high power density and long cycle lifetime [18]. They are used in electric and hybrid vehicles [19, 20], power electronics [21], and industrial power management [22]. Porous electrode materials with high surface area are typically used to achieve large power and energy densities [17, 23]. Amorphous nanoporous carbons are attractive for EDLC electrode materials due to their large electrical conductivity, surface area, and temperature stability as well as for their relatively low cost [22, 24, 25]. They include activated carbon [18], carbon black [25], carbide derived carbon [26], and carbon aerogels [27]. Under normal operation, EDLCs are charged and discharged under high currents responsible for heat generation within the electrolyte and the electrode [19, 28]. High operating temperatures may result in shorter lifespans, higher pressure within the EDLC, and evaporation of the electrolyte [20]. Thus, thermal management of EDLCs is crucial for their performance and reliability [19]. Several thermal models of EDLCs have been developed [19, 20, 28–31]. All of them require the effective thermal conductivity of the nanoporous carbon electrode as an input parameter.

The thermal conductivity of hydrogenated and hydrogen-free non-porous a-C thin films has already been measured at room temperature [15, 16] and between 80 and 400 K [6, 7]. However, the effective thermal conductivity of amorphous nanoporous carbons at 300 K has been investigated by a limited number of studies of carbon aerogels [10, 11].

The present study aims to elucidate the effects of nanoporosity on the thermal conductivity of nanoporous amorphous carbon at 300 K using equilibrium molecular dynamics (MD) simulations. A wide range of system length, pore diameter, porosity, and effective density were considered. The results are compared with effective medium approximations (EMAs) from the literature [34–38].

2 Background

2.1 Amorphous carbon

Carbon atoms in amorphous carbon exhibit three types of bond hybridization, namely sp^3, sp^2, and sp^1 [1]. In the sp^3 hybridization, four valence electrons form tetrahedrally-directed σ bonds, the strongest type of covalent bonds. The sp^2 configuration is composed of three valence electrons forming trigonally-directed σ bonds, while the fourth forms a weak covalent π bond normal to the σ-bonding plane. The sp^1 configuration forms two planar σ bonds and two π bonds in the orthogonal planes [1, 39]. Diamond features solely sp^3 hybridization whereas graphite is comprised of sp^2 bonds. Amorphous carbon consists of a mix of sp^3, sp^2, and sp^1 hybridizations characterized by the average coordination number $\langle n \rangle$. The coordination number of a given atom is the number of nearest neighboring atoms. The sp^3, sp^2, and sp^1 configurations correspond to an average coordination number $\langle n \rangle$ equal to 4, 3, and 2, respectively [1].

Figure 1 shows the ternary phase diagram of amorphous carbon with sp^3 and sp^2 hybridization with hydrogenation [1]. Hydrogen-free *a*-C is categorized as either tetrahedral amorphous carbon *ta*-C, sometimes referred to as amorphous diamond *a*-D, or as graphite-like amorphous carbon (GLC) [39]. The *ta*-C phase features 65-90% sp^3 hybridization compared with 0-35% for GLC [39]. Often, a hydrocarbon precursor is used in the deposition process resulting in hydrogenated amorphous carbon [1]. Then, hydrogenated amorphous carbon *a*-C:H can be classified into four types: (i) polymer-like *a*-C:H (PLCH) with the highest H-content between 40 and 60 at. %, and up to 70% sp^3 bonds [40], (ii) diamond-like *a*-C:H (DLCH) with 20-40 at. % H [40] and 20-60% sp^3 bonds [6], (iii) *ta*-C:H with 25-30 at. % H and 65-90% sp^3 bonds [39], and (iv) graphite-like *a*-C:H (GLCH) with H-content less than 20 at. % and sp^3 content between 0 and 39% [39].

Material properties, such as hardness, optical band gap, density, and thermal conductivity, depend on the bond hybridization of carbon [6, 39, 41]. For instance, Ferrari *et al.* [41] determined that the density of *ta*-C and *ta*-C:H increased with increasing sp^3 hybridization.

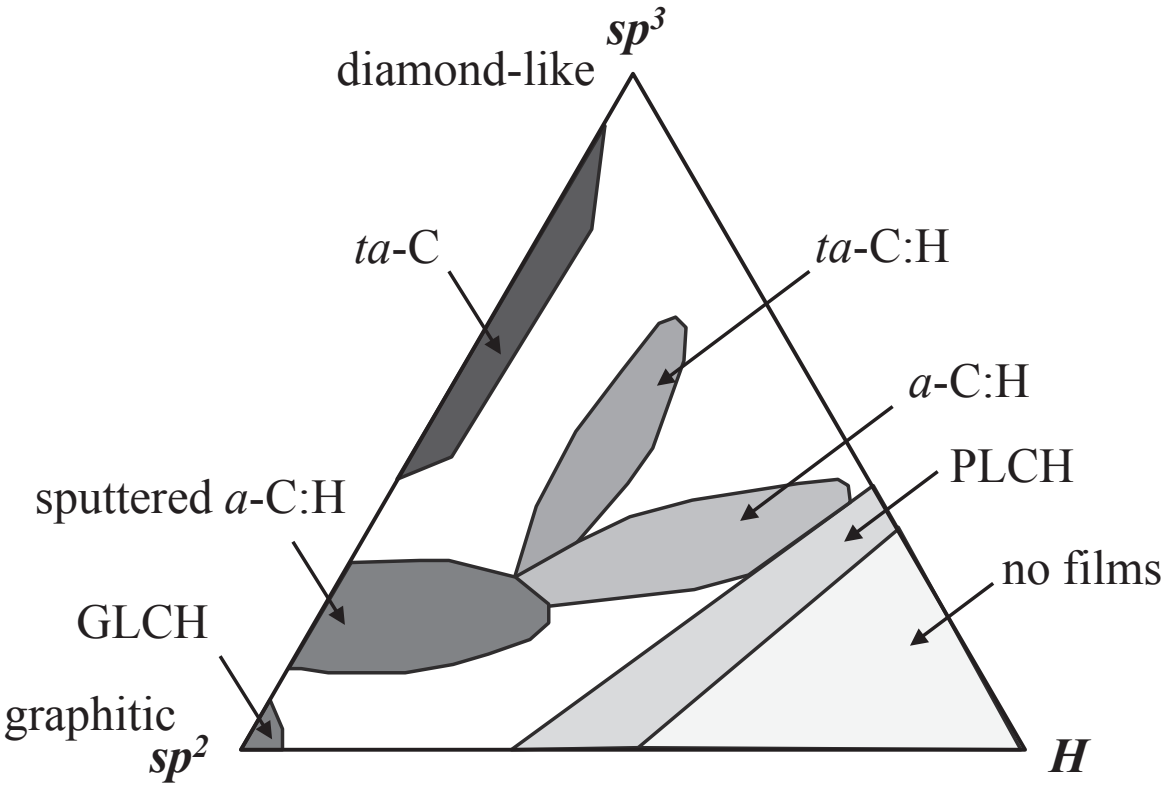

Figure 1: Ternary phase diagram for amorphous carbon relating sp^2, sp^3, and hydrogen content [1].

On the contrary, the authors found that sp^3 hybridization in *a*-C:H increased due to increasing hydrogen content and resulted in decreasing density. Shamsa *et al.* [6] observed that the thermal conductivity of *a*-C and *a*-C:H increased with sp^3 content, or structural disorder, quantified by Raman spectroscopy.

Deposition methods of amorphous carbon films largely control their sp^3 and hydrogen content. Pulsed laser deposition (PLD) [15], ion-beam sputter deposition (IBSD) [15], direct ion beam deposition (DIBD) [15], cathodic arc deposition (CAD) [15], filtered arc deposition (FAD) [7], filtered cathodic vacuum arc (FCVA) [6], and filtered high current pulsed arc (HCA) [6] have been used to deposit *ta*-C films. Alternatively, electron cyclotron wave resonance (ECWR) can be used to deposit *ta*-C:H films [1,6]. Sputtering is commonly used to deposit both hydrogenated and hydrogen-free amorphous carbon [6]. Plasma enhanced chemical vapor deposition (PECVD) is widely used to deposit hydrogenated amorphous

carbon films with low sp^3 content [1, 6, 16]. In addition, plasma assisted chemical vapor deposition (PACVD) [7, 15] and remote-plasma chemical vapor deposition (RPCVD) [7] generate *a*-C:H films with significant hydrogen content, typically around 30 at. % H [7, 15].

2.2 Molecular dynamics simulations

2.2.1 Methods for predicting thermal conductivity

MD simulations model a system of atoms by solving Newton's equations of motion for each atom whose interatomic interactions are governed by semi-empirical potential functions. They can be used to determine the thermal conductivity of a material based on either the non-equilibrium method [42] or the equilibrium method [43, 44]. Schelling *et al.* [45] demonstrated that these two methods were equivalent for bulk silicon at 500 K. In the non-equilibrium Müller-Plathe method, a heat flux is imposed by swapping the velocities of atoms in a designated cold slab with those from a hot slab [42]. This known heat flux and the resulting temperature gradient can be used to compute the thermal conductivity using Fourier's law [42]. Alternatively, the equilibrium method relates a system's thermal conductivity k to the heat current autocorrelation function (HCACF) $\langle J(0)J(t)\rangle$ where $J(t)$ is the heat current, using the Green-Kubo relation given by [46]

$$k = \frac{1}{3Vk_BT^2}\int_0^\infty \langle J(0)J(t)\rangle \,\mathrm{d}t \tag{1}$$

where V is the volume of the system simulated, $k_B = 1.38 \times 10^{-23}$ J/K is the Boltzmann constant, and T is the system temperature. At equilibrium, fluctuations in the temperature of the system induce a time-dependent heat current $J(t)$ (in J·m/s) and the thermal conductivity dictates the response of the system to these fluctuations. In materials with large thermal conductivity the fluctuations dissipate slowly, so the HCACF persists for a relatively long time. In low thermal conductivity materials, fluctuations dissipate quickly so the HCACF is short lived [12].

In practice, the upper limit of the integral in Equation (1) is replaced by the maximum correlation time τ_{max} [47]. The latter is chosen to be larger than the required time for the

HCACF to decay to zero [45]. Schelling *et al.* [45] found that, for short correlation times ($\tau <$ 0.2 ps), the HCACF decayed quickly. However, extending the correlation time demonstrated that the HCACF did not decay to zero until $\tau = 100$ ps. Similarly, Che *et al.* [48] saw an initial decay after $\tau = 50$ fs and a decay to zero after $\tau = 30$ ps for diamond at 300 K. Earlier studies [48–50] fitted the HCACF to an exponential decay using a shorter correlation time than that required for the HCACF to decay to zero. This reduced the overall simulation time compared to direct integration in Equation (1). However, Schelling *et al.* [45] showed that an exponential fit resulted in significant underprediction of the thermal conductivity. Therefore, the procedure prescribed by Schelling *et al.* [45] using the direct integration of $\langle J(0)J(t)\rangle$ of Equation (1) was used in this study.

2.2.2 Interatomic potentials

A variety of empirical interatomic potentials have been developed for carbon systems [51]. The Tersoff potential was developed for covalent systems, including silicon and carbon, and named after its author [5, 52]. It accurately predicted elastic constants and phonon frequencies in diamond as well as defect energies in diamond and graphite [5]. The Tersoff potential is given by [5]

$$E = \frac{1}{2}\sum_{i \neq j} f_C(r_{ij}) \left[a_{ij} E_R(r_{ij}) + b_{ij} E_A(r_{ij})\right] \tag{2}$$

where f_C is a smoothing cutoff function, E_R is a repulsive pair potential, E_A is an attractive pair potential, a_{ij} limits the interaction with the first neighbor shell, b_{ij} is a measure of bond order, and r_{ij} is the distance between atoms i and j.

The environmental-dependent interaction potential (EDIP) was developed for carbon by Marks [53]. It accurately predicted elastic constants of diamond and graphite and radial and angle distribution functions of amorphous carbon. However, it does not predict correct distances for double and triple carbon-carbon bonds [51, 53]. The EDIP is given by [53]

$$E = \sum_{i \neq j} E_2(r_{ij}, Z_i) + \sum_{i \neq j} \sum_{i \neq k, k > j} E_3(r_{ij}, r_{ik}, \theta_{jik}, Z_i) \tag{3}$$

where E_2 is a pair potential and E_3 is a three-body potential, Z_i is the effective coordination number of atom i, and θ_{jik} is the angle between atom j and atom k subtended at atom i.

The reactive empirical bond order (REBO) potential developed by Brenner [54, 55] and its variants are among the most widely used potentials. The first generation REBO potential [54,55] was used to model various carbon and hydrocarbon systems such as pyrolitic chars [8], diamond [48], and graphene [56]. Subsequently, Brenner *et al.* [57] modified the REBO potential to more accurately predict energetic, elastic, and vibrational properties of carbons and hydrocarbons. Stuart *et al.* [4] introduced intermolecular and torsional interactions to the REBO potential E_{REBO} to develop the adaptive intermolecular REBO (AIREBO) potential given by [4]

$$E = E_{REBO} + E_{LJ} + E_{tors} \tag{4}$$

where E_{LJ} represents Lennard-Jones intermolecular interactions and E_{tors} accounts for torsional interactions [4]. The AIREBO potential successfully modeled structural, mechanical, and energetic properties of diamond and graphite [4]. It was also used to model the structure of amorphous carbon at 300 K with density ranging from 2.0 to 3.0 g/cm^3 [58].

2.2.3 Thermal conductivity of amorphous carbon

Very few MD simulation studies have considered the thermal conductivity of amorphous carbon [8, 9]. Makeev *et al.* [8] investigated the dependence of thermal conductivity of pyrolitic chars on temperature and average coordination number using non-equilibrium MD (NEMD) simulations. The authors used the first generation REBO potential [54, 55] to model interatomic interactions. The temperature varied from 25 to 500 K and the average coordination number $\langle n \rangle$ ranged from 2.93 to 3.10, i.e., the carbon atoms were largely sp^2 hybridized. Makeev *et al.* [8] found their predictions to be in good agreement with the minimum thermal conductivity model [59] given by [59, 60],

$$k_{min} = \left(\frac{\pi}{6}\right)^{1/3} k_B n_0^{2/3} \sum_{i=1}^{3} v_i \left(\frac{T}{\Theta_i}\right)^2 \int_0^{\frac{\Theta_i}{T}} \frac{x^2 e^x}{(e^x - 1)^2} \, \mathrm{d}x \tag{5}$$

where n_0 is the number density of atoms, T is the absolute temperature, and i is the index of the three acoustic phonon modes with group velocity v_i and cutoff temperature $\Theta_i = v_i(\hbar/k_B)(6\pi^2 n_0)^{1/3}$. Here, $\hbar = 1.05 \times 10^{-34}$ J·s is Planck's constant divided by 2π. The speed of sound for transverse v_t and longitudinal v_ℓ phonon modes were expressed as [8]

$$v_t = \sqrt{\frac{Y}{2(1+\nu)}} \qquad v_\ell = v_t\sqrt{\frac{2(1-\nu)}{1-2\nu}} \tag{6}$$

where Y and ν are the Young's modulus and Poisson's ratio, respectively. In order to predict the dependence of thermal conductivity on coordination number using the minimum thermal conductivity model, Makeev *et al.* [8] related the density to the average coordination number $\langle n \rangle$ using a linear relation suggested by Mathioudakis *et al.* [61] expressed as

$$\rho = 1.65\langle n \rangle - 3.29. \tag{7}$$

where ρ is given in g/cm^3. The density ρ is related to the number density n_0 by

$$\rho = MN_A n_0 \tag{8}$$

where M is the molar mass of the atom and $N_A = 6.022\times10^{23}$ at/mol is Avogadro's constant. They found that the thermal conductivity increased with temperature and average coordination number or increasing density.

Suarez-Martinez *et al.* [9] investigated the effect of microstructure on the thermal conductivity of amorphous and glassy carbon at room temperature using the environment-dependent interaction potential (EDIP) and non-equilibrium MD simulations [53]. The density spanned 1.4 to 3.0 g/cm^3 and carbon atoms were primarily sp^2 hybridized. The density of amorphous carbon was found to scale linearly with sp^3 bond fraction. Thermal conductivity depended linearly on density. This was in qualitative agreement with thermal conductivity data predicted by Makeev *et al.* [8] for pyrolitic chars. However, both of these MD simulations studies [8,9] predicted thermal conductivities larger than most experimental measurements [6, 7, 16].

2.3 Experimental measurements

Table 1 summarizes thermal conductivity measurements reported in the literature for non-porous amorphous carbon thin films [6, 7, 15, 16] and for carbon aerogels [10, 11].

Table 1: Summary of experimental studies of dense amorphous carbon thin films [6, 7, 15, 16] and carbon aerogels [10, 11]

Ref.	**Film Type**	**Synthesis method**	**T (K)**	ρ **(g/cm^3)**	**Thickness**	**Measurement method**	sp^3	**at. % H**	**k (W/m·K)**
[15]	*ta*-C	PLD, CAD, IBSD,	Room T	2.7-3.2	69-150 nm	optical	N/A	0	5.2-9.7
[7]		FAD	80-400	2.3-2.8	20 - 48 μm	3ω	30-80%	0	1.3-2.5
[6]		FCVA, HCA	80-400	2.59-3.26	18.5-100 nm	3ω	–	0	1.41-3.5
[6]	*ta*-C:H	ECWR	80-400	2.2-2.4	18.5-100 nm	3ω	70%	28-30	0.77-1.3
[16]	*a*-C:H	PECVD	Room T	1.0-1.4	450-800 nm	optical	20-80%	27-42	0.65-1.4
[15]		dc-PACVD, DIBD	Room T	1.7	100-300 nm	optical	N/A	0-37	0.28-0.95
[6]		PECVD, FCVA,	80-400	1.55-2	18.5-100 nm	3ω	<20-70%	18-36	0.248-0.69
[7]		RPCVD, PACVD	80-400	0.9-2.1	120 nm -108 μm	3ω	30-80%	33-50	0.20-1.1
[11]	Carbon aerogel*	$T_p = 1050°C$,	300- 973	0.381-0.984	0.6-1.0 mm	laser flash	N/A	0	0.35-2.75
[10]		$T_p = 1050°C$,	Room T	0.06-0.650	1.5 cm	transient	N/A	0	0.02-0.35

* from resorcinol-formaldehyde aerogel

2.3.1 Nonporous amorphous carbon films

One of the earliest thermal conductivity measurements of amorphous carbon films was performed by Morath *et al.* [15] on *ta*-C and *a*-C:H with film thickness ranging from 100 to 300 nm. The authors estimated thermal conductivity at room temperature using the optical pump-probe technique. This method requires estimates of density, molecular weight, and Poisson's ratio in order to determine the film thermal conductivity [15]. The densities of the *ta*-C films were approximately 2.7, 3.0, and 3.2 g/cm^3 [63, 64] and the corresponding thermal conductivity ranged from 5.2 to 9.7 W/m·K. The film with the lowest density had the smallest thermal conductivity. However, that with the largest density did not have the largest thermal conductivity. On the other hand, the density of *a*-C:H films was not measured by Morath *et al.* [15] but rather was assumed to be 1.7 g/cm^3 based on a previous study of a similar film [65]. Morath *et al.* [15] measured the thermal conductivity of *a*-C:H to be between 0.28 to 0.95 W/m·K. These variations were due to differences in hydrogen content which ranged from 28 to 37 at. % H. However, it is unclear if the order of magnitude decrease in thermal conductivity between *ta*-C and *a*-C:H could be attributed to (i) difference in density, (ii) hydrogenation, and/or (iii) differences in sp^3 hybridization.

Subsequent experimental studies [6, 7, 16] were in good agreement with the thermal conductivity reported by Morath *et al.* [15] for *a*-C:H films but reported significantly smaller thermal conductivity for *ta*-C films. Bullen *et al.* [7] measured the thermal conductivity of *a*-C and *a*-C:H films deposited on silicon substrates between 80 and 400 K using the 3ω method accounting for the contact resistance between film and substrate. The films' densities varied between 0.9 and 2.8 g/cm^3 and their thicknesses ranged from 120 nm to 108 μm. At 300 K, the thermal conductivity ranged from 0.20 to 2.5 W/m·K. The authors determined that the thermal conductivity increased with increasing density for both *a*-C and *a*-C:H.

Shamsa *et al.* [6] measured the thermal conductivity of a variety of *ta*-C and *a*-C films, deposited on a silicon substrate, between 80 and 400 K. The film samples featured (i) sp^3 content ranging from less than 20% up to 70%, (ii) density between 1.55 and 3.26 g/cm^3, and (iii) thickness from 18.5 to 100 nm. Although the films were thin, the authors did not

correct for interfacial thermal contact resistance between the films and the substrate. The hydrogen content varied between 0 and 36 at. % H and the thermal conductivity ranged from 0.25 to 3.5 W/m·K at 300 K. Here also, the thermal conductivity of *ta*-C and *a*-C films increased with increasing film density. Shamsa *et al.* [6] fitted their experimental data for thermal conductivity k of *a*-C at 300 K as a linear function of density ρ according to

$$k = 1.77\rho - 2.82 \tag{9}$$

where k and ρ are expressed in W/m·K and g/cm^3, respectively. However, this linear fit predicts negative effective thermal conductivity for effective density less than 1.59 g/cm^3. In addition, below 2.0 g/cm^3 the dependence of k on ρ was unclear and the thermal conductivity k did not necessarily increase with increasing density ρ. For example, a film with density of 2.0 g/cm^3 and 24 at. % H had a lower thermal conductivity than that with density of 1.8 g/cm^3 and 18 at. % H. This suggests that increasing hydrogenation reduces thermal conductivity as demonstrated using MD simulations of hydrogenated graphene [56, 62]. Shamsa *et al.* [6] also showed that thermal conductivity increased linearly with structural disorder, measured using Raman spectroscopy and previously shown to increase with increasing sp^3 content [40]. Thus, the authors concluded that thermal conductivity was linearly proportional to sp^3 content.

Arlein *et al.* [16] experimentally studied *a*-C:H films deposited on a silicon substrate with density between 1.0 to 1.4 g/cm^3 and thickness varying from 450 to 800 nm. The films' thermal conductivity was measured using the optical pump-probe method at room temperature and ranged from 0.65 to 1.4 W/m·K. However, unlike other experimental results [6, 15], the *a*-C:H film thermal conductivity k was not found to increase with increasing density and decreasing hydrogen content. In addition, no expression for the thermal conductivity was derived [16] . The authors reported an overall experimental uncertainty of ±15% in the thermal conductivity due to characterization and measurements but did not state whether the contact resistance had been accounted for.

Overall, the above reviewed experimental studies led to contradictory conclusions on the effects of density and hydrogen content on the thermal conductivity of amorphous carbon.

However, the thermal conductivity of hydrogen-free amorphous carbon generally increased with increasing density.

2.3.2 Carbon aerogels

Carbon aerogels are low density nanoporous amorphous carbon materials produced by pyrolysis featuring porosity between 80 and 90% [66] and polydisperse pores with diameter ranging from 1 to 100 nm [11]. Pyrolysis temperature T_p significantly affects the thermal conductivity of aerogels for a given density [67]. For example, Wiener *et al.* [67] found that the effective thermal conductivity k_{eff} of carbon aerogels with porosity of 85% in a vacuum at 300°C increased from 0.05 to 0.42 W/m·K as the pyrolysis temperature T_p increased from 800 to 2500°C. This was attributed to the fact that carbon aerogels pyrolized at high temperatures had less defects and hence larger phonon mean free path and thermal conductivity. In other words, higher pyrolysis temperatures cured defects responsible for phonon scattering [67]. The effective density was found to be independent of pyrolysis temperature. On the contrary, pore size decreased and specific surface area increased as pyrolysis temperature increased from 800°C to 1000°C. However, it was the reverse for pyrolysis temperature T_p above 1000°C.

Lu *et al.* [10] measured, at room temperature and under low pressure, the thermal conductivity of carbon aerogels pyrolized at 1050°C. For a pressure of 0.02 mbar, the authors found that the effective thermal conductivity k_{eff} was proportional to $\rho_{eff}^{1.5}$, where ρ_{eff} was the carbon aerogel effective density. Bock *et al.* [11] also measured the thermal conductivity of carbon aerogels pyrolized at 1050°C for temperatures ranging from room temperature to 700°C. The effective density ρ_{eff} varied between 0.381 and 0.984 g/cm^3. At room temperature and pressure less than 1 mbar, the effective thermal conductivity ranged from 0.21 to 1.72 W/m·K and was proportional to $\rho_{eff}^{2.2}$.

2.4 Physical modeling

Effective medium approximations (EMAs) from the literature generally describe the effective thermal conductivity k_{eff} of porous amorphous materials in terms of (i) the porosity f_v, (ii) the thermal conductivity of the continuous amorphous matrix k_c, and (iii) the thermal conductivity of the dispersed gas phase k_d [12, 34–38, 68–70].

The thermal conductivity of the gas phase entrapped in a pore of diameter d_p is related to the Knudsen number Kn according to [12, 71]

$$k_d = \frac{k_{d,0}}{1 + 1.5\beta \mathrm{Kn}} \qquad \text{where} \qquad \mathrm{Kn} = \frac{\ell}{d_p} = \frac{k_B T}{\sqrt{2}\pi\sigma^2 p d_p}. \tag{10}$$

where, $k_{d,0}$ is the thermal conductivity of the bulk gas phase, $k_B = 1.38 \times 10^{-23}$ J/K is the Boltzmann constant, ℓ is the mean free path of the gas at temperature T and pressure p inside the pores, while σ is the diameter of the gas molecules treated as hardshell particles. For bulk air at room temperature and atmospheric pressure, $k_{d,0}$ is taken as 0.026 W/m·K and the coefficient β is equal to 1.5 for entrapped air [12]. In the experimental studies previously reviewed [10, 11], the pressure was less than 1 mbar, so Kn was very large and k_d was negligibly small. Note that the contribution of radiation transfer to the effective thermal conductivity can be neglected due to carbon's large specific extinction coefficient [10].

The parallel model is a simple and commonly used two-phase effective medium approximation (EMA) given by [34, 35]

$$k_{eff} = k_c(1 - f_v) + k_d f_v. \tag{11}$$

In addition, Maxwell Garnett [36] developed an EMA for the effective dielectric constant of inclusions embedded in a matrix. It has since been used to model other effective physical properties, including the effective thermal conductivity [72]. For a porous matrix, with $k_d = 0$ W/m·K, the Maxwell Garnett model for the effective thermal conductivity k_{eff} can be written as [36],

$$k_{eff} = 2k_c \left(\frac{1 - f_v}{2 + f_v} \right). \tag{12}$$

This EMA is equivalent to the Hamilton model [73] for the thermal conductivity of porous media with spherical pores. Note that Coquil *et al.* [12] found this model to be in very good

agreement with the effective thermal conductivity of nanoporous amorphous silica at 300 K predicted by solving Fourier's law in a continuous matrix containing ordered spherical pores with simple cubic packing arrangements. This was also established analytically based on the method of volume averaging [69].

Landauer [37] developed an EMA for the effective thermal conductivity k_{eff} of spherical inclusions in a matrix expressed as,

$$4k_{eff} = (3f_v - 1)k_d + (2 - 3f_v)k_c + \{[(3f_v - 1)k_d + (2 - 3f_v)k_c]^2 + 8k_c k_d\}^{1/2}. \quad (13)$$

In the limiting case when k_d goes to zero, Equation (13) simplifies to the so-called coherent potential model, also equivalent to the symmetric Bruggeman model [70], and given by

$$k_{eff} = k_c(1 - 1.5f_v). \quad (14)$$

Cahill [74] found the effective thermal conductivity of Vycor glass, with 30% porosity containing pores approximately 10 nm in size, to be in good agreement with Equation (14) for temperatures ranging between 30 and 300 K. Moreover, previous MD simulations of the effective thermal conductivity of nanoporous amorphous silica at 300 K were found to be in good agreement with Equation (14) for porosity f_v ranging from 0 to 35% [12]. However, note that Equation (14) predicts negative effective thermal conductivity for porosity f_v larger than 67%.

Looyenga [38] developed an EMA for the effective dielectric constant. This EMA has also been used to model the effective thermal conductivity in porous materials [75, 76]. It has been referred to as the percolation model and is given by

$$k_{eff} = k_c(1 - f_v)^3. \quad (15)$$

Note that the effective thermal conductivity of carbon aerogels was generally reported as a function of effective density ρ_{eff} rather than porosity f_v [10, 11]. Assuming that the density of the gas phase ρ_d was negligible compared with that of the dense matrix phase ρ_c the effective density ρ_{eff} of a porous medium can be expressed as

$$\rho_{eff} = \rho_c(1 - f_v). \quad (16)$$

Unfortunately, experimental studies reporting the effective thermal conductivity of carbon aerogels as a function of their effective density ρ_{eff} did not report the density ρ_c and thermal conductivity k_c of the continuous phase [10, 11]. Therefore, the aforementioned EMAs could not be compared with experimental measurements [10, 11].

In the present study, equilibrium MD simulations based on the Green-Kubo method were used to predict the effective thermal conductivity at 300 K of nanoporous amorphous structures with various porosity resulting in different effective density. The AIREBO potential was used to model C-C atomic interactions. The results were compared with existing EMAs and thermal models [8, 9] along with experimental data reported for nonporous amorphous carbon and carbon aerogels [6, 7, 10, 11, 15, 16].

3 Procedure

Figure 2a shows the crystalline diamond precursor from which the amorphous carbon, shown in Figure 2b, was derived. Figures 2c and 2d show the porous amorphous carbon structure with 30% porosity in 3D and 2D, respectively. The numerical procedures for amorphization, pore insertion, and the corresponding prediction of the thermal conductivity were implemented using the Large-scale Atomic/ Molecular Massively Parallel Simulator (LAMMPS) [77]. Simulations were run in parallel on fifty 64-bit nodes with 4000 MB of RAM. Each structure was simulated seven different times to estimate the average thermal conductivity and the error bars corresponding to 95% confidence interval.

3.1 Hydrogen-free nonporous amorphous carbon

Amorphous carbon was simulated by first generating a crystalline diamond structure consisting of a diamond cubic unit cell repeated six to eight times in the x-, y-, and z-directions. A diamond unit cell contains eight carbon atoms and has a density of 3.54 g/cm^3 and lattice constant of 3.57 Å [48]. The previously mentioned AIREBO potential was used to model C-C interactions [4]. All boundary conditions were periodic to simulate bulk materials. Once the crystalline matrix was constructed, an energy minimization step was performed to relax

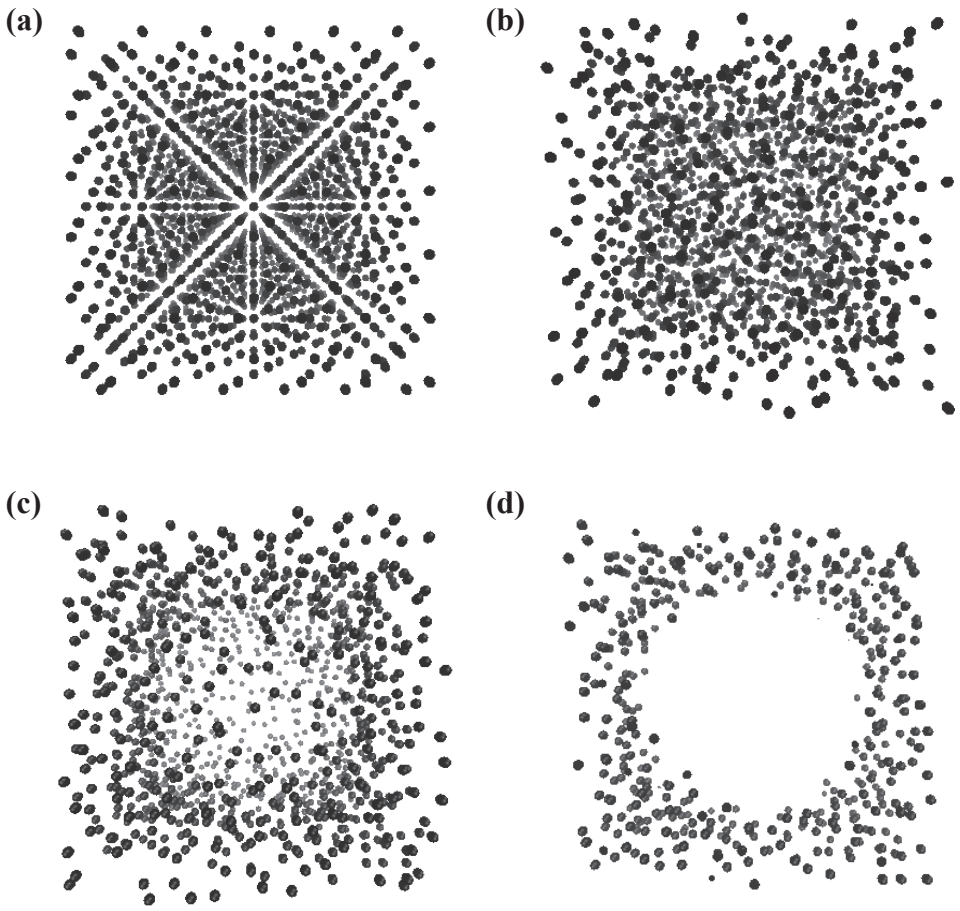

Figure 2: Atomic structures of (a) the crystalline diamond precursor from which amorphous carbon was derived, (b) the nonporous amorphous carbon, (c) the porous amorphous carbon with 30% porosity in 3D, and (d) in 2D.

the system.

In order to generate an amorphous carbon structure, the crystalline diamond structure was heated to 15,000 K and then cooled to 300 K for 300,000 time steps, using a Nosé-Hoover thermostat [78, 79]. For a given amorphous structure, Newton's equations of motion for each atom were solved with a time step Δt and were integrated using a velocity Verlet integrator [80]. This quench rate of 500 K/ps was previously used by Stuart *et al.* [58], although the authors only heated the crystalline structure to 5,000 K. In the present study, the crystalline structures quenched from 5,000 K featured thermal conductivity one order of magnitude larger than those quenched from 15,000 K at the same quenching rate of 500

K/ps. In addition, a system quenched from 20,000 K was found to have similar thermal conductivity as those quenched from 15,000 K. This suggests that the carbon structure generated via heating to 15,000 K was fully amorphous. Thus, all results presented here have been obtained using the amorphization procedure at 15,000 K. The density of the amorphous system generated was 3.54 g/cm^3. Three other systems with lower densities of 2.66, 2.05, and 1.61 g/cm^3 were generated by isotropically expanding the simulation cell of the amorphous structure.

The thermal conductivity of the different amorphous structures at 300 K was computed using the Green-Kubo relation [Equation (1)] for a maximum correlation time averaging window $\Delta\tau_{max}$, total simulation time t_{max}, and system length L under constant number of atoms, volume, and temperature (NVT ensemble).

Figure 3 plots the thermal conductivity k_c of amorphous carbon with density ρ_c of 3.54 g/cm^3 at 300 K as a function of time step Δt between 0.05 and 0.2 fs. Here, the maximum correlation time averaging window $\Delta\tau_{max}$ was between 4 and 8 ps, the total simulation time t_{max} was 4.5 ns, and the system length L was 21.3 Å. The thermal conductivity computed for a time step of 0.1 fs was nearly identical to that obtained using 0.05 fs. The results for the different values of Δt fell within each other's numerical uncertainty. However, increasing the time step to 0.2 fs produced large numerical uncertainties. Thus, a 0.1 fs time step was used for all simulations reported in this study.

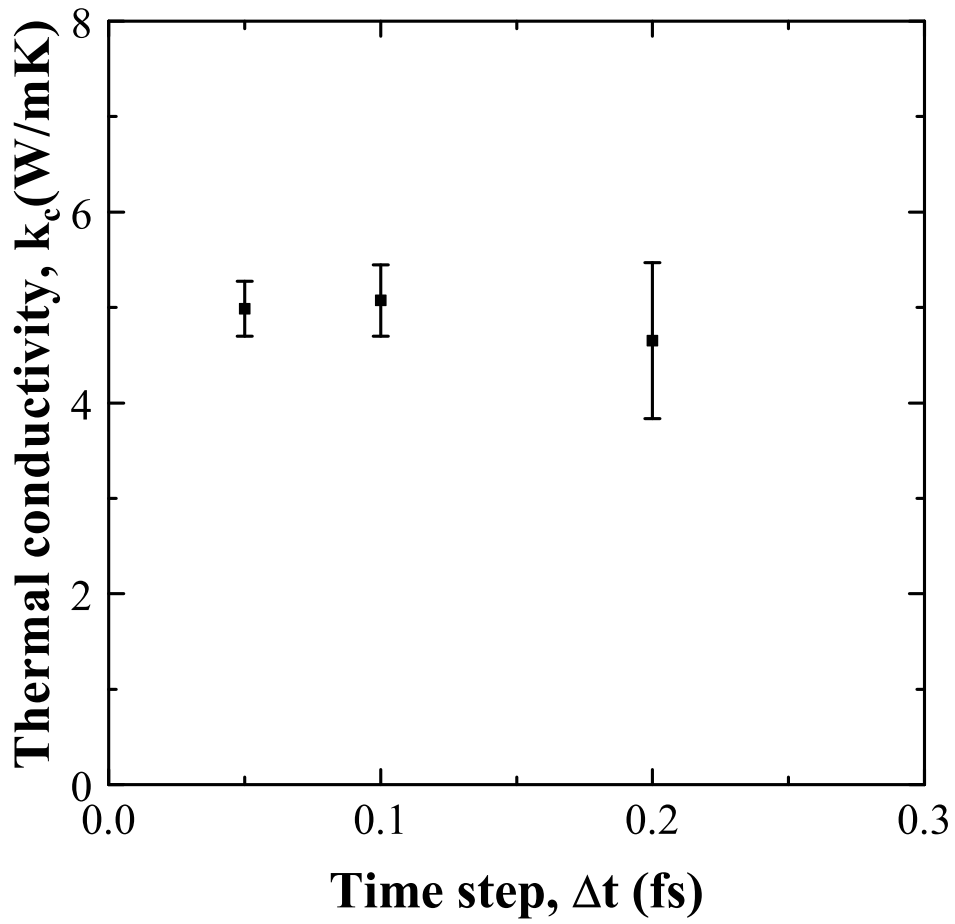

Figure 3: Thermal conductivity k_c of hydrogen-free nonporous amorphous carbon with density ρ_c of 3.54 g/cm^3 at 300 K as a function of time step Δt for a maximum correlation time averaging window $\Delta\tau_{max}$ between 4 and 8 ps, total simulation time t_{max} of 4.5 ns, and system length L of 21.3 Å.

Figures 4a and 4b respectively plot the normalized HCACF $\langle J(t)J(0)\rangle/\langle J(0)J(0)\rangle$ and the thermal conductivity k_c of amorphous carbon at 300 K with a density ρ_c of 1.61 g/cm^3 as functions of the correlation time τ ranging from 0 to 10 ps using a time step Δt of 0.1 fs, a total simulation time t_{max} of 4.5 ns, and a system length L of 27.8 Å. Recall, the maximum correlation time τ_{max} is selected to be larger than the correlation time τ required for the HCACF to decay to zero [45]. In other words, the thermal conductivity corresponding to the maximum correlation time τ_{max} is equal to that corresponding to correlation times τ larger than τ_{max}. Figure 4a indicates that the HCACF decayed to zero when the correlation

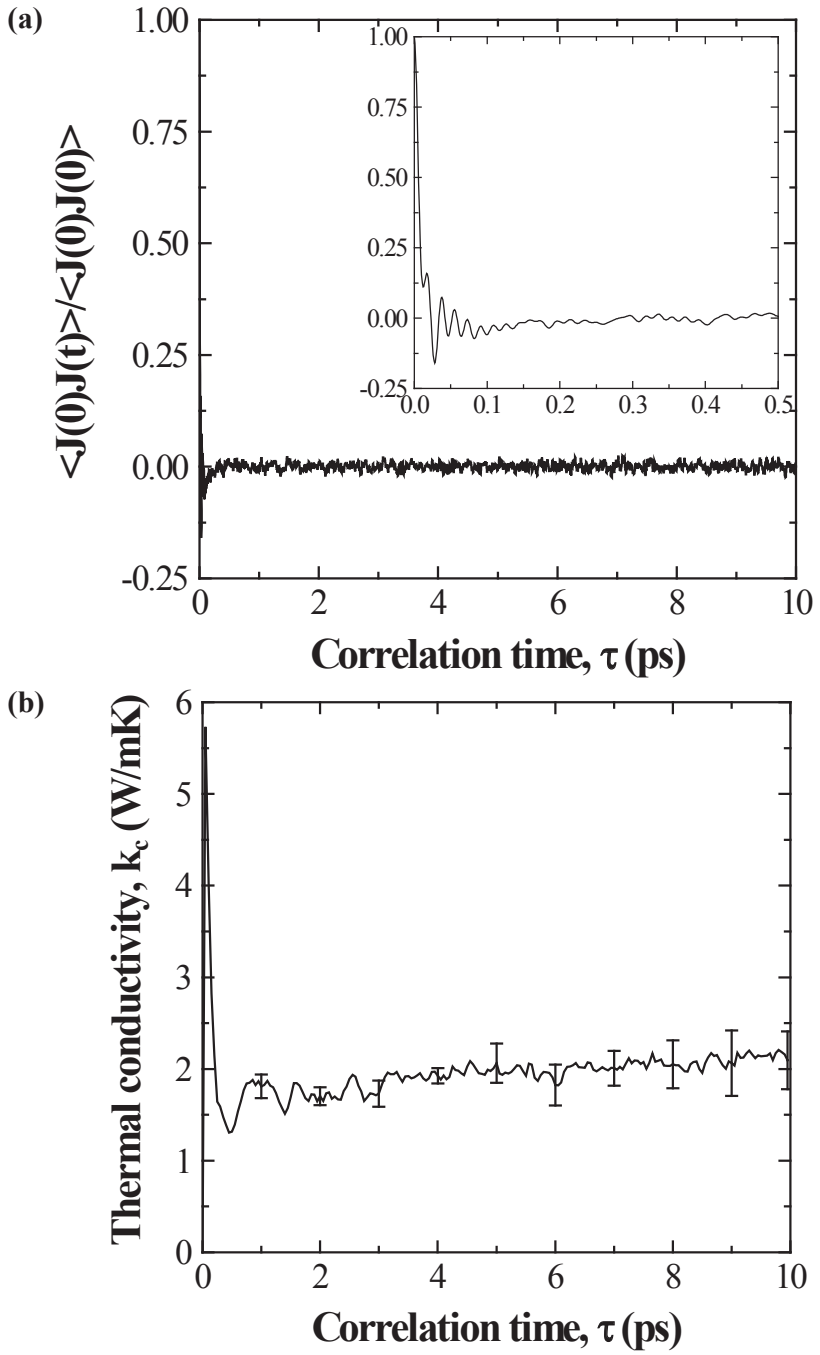

Figure 4: (a) Normalized HCACF and (b) thermal conductivity k_c as functions of correlation time τ for hydrogen-free nonporous amorphous carbon with density ρ_c of 1.61 g/cm^3 at 300 K for a time step Δt of 0.1 fs, total simulation time t_{max} of 4.5 ns, and system length L of 27.8 Å.

time τ was longer than 0.3 ps. However, Figure 4b shows that the thermal conductivity did not converge until the correlation time was longer than 4 ps. Note that for larger densities, the thermal conductivity converged for shorter correlation times. Figure 4b also indicates that after the thermal conductivity had converged ($\tau > 4$ ps), it fluctuated about an average value. Thus, the average thermal conductivity was obtained by averaging the results from Equation (1) using a range of maximum correlation times τ_{max}, or a maximum correlation time averaging window $\Delta\tau_{max}$ of 4 to 8 ps. As discussed previously, Schelling *et al.* [45] determined that for a silicon system at 500 K the HCACF decayed rapidly for short correlation times ($\tau < 0.2$ ps), while correlations persisted for much longer ($\tau > 100$ ps). To ensure that correlations did not persist for correlation times longer than 4 ps, a maximum correlation time of 100 ps was considered. No difference was found between the thermal conductivity predicted using τ_{max} of 4 ps and 100 ps.

The total simulation time t_{max} should be much larger than the maximum correlation time τ_{max} to ensure proper statistical averaging [45]. Figure 5 shows the thermal conductivity k_c for total simulation time t_{max} ranging from 4.1 to 6.0 ns for hydrogen-free nonporous amorphous carbon with density of 1.61 g/cm^3, time step Δt of 0.1 fs, a maximum correlation time τ_{max} averaging window ranging from 4 to 8 ps, and a system length L of 27.8 Å. It indicates that the value of thermal conductivity was converged for a total simulation time t_{max} of 4.5 ns. For larger densities, convergence was achieved for shorter simulation times so that a total simulation time t_{max} of 4.5 ns was used for all MD simulations of nonporous amorphous carbon.

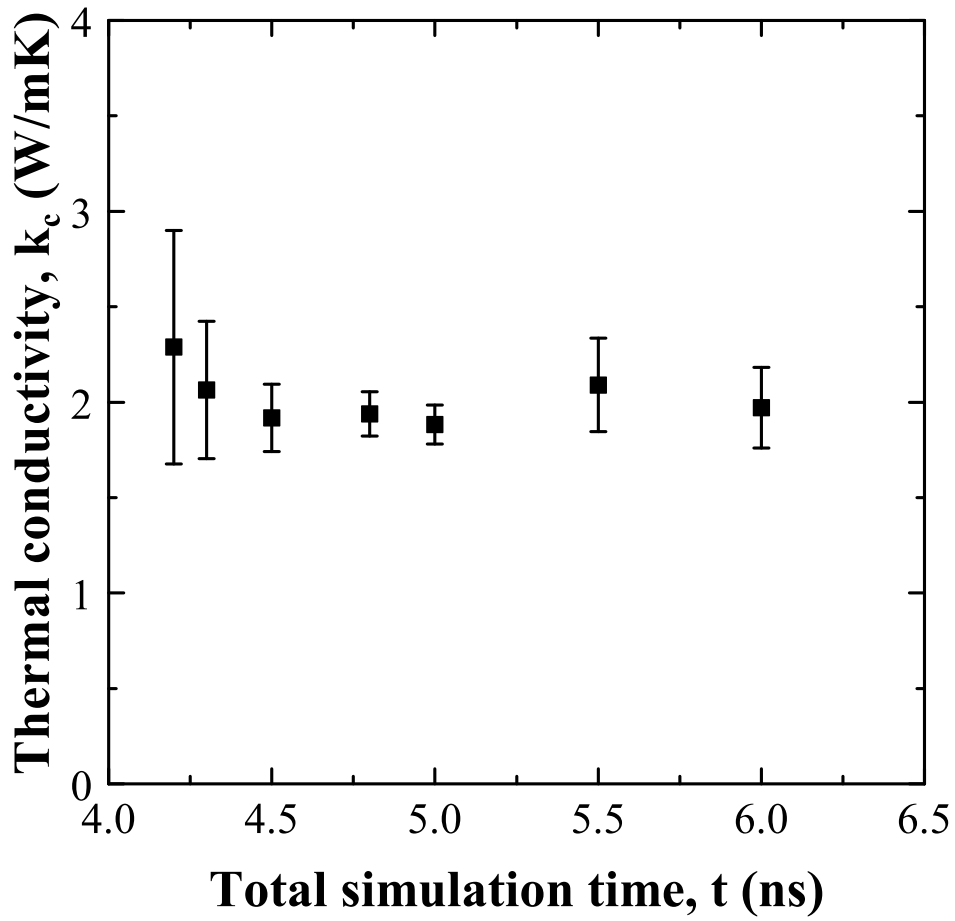

Figure 5: Thermal conductivity k_c of hydrogen-free nonporous amorphous carbon with density ρ_c of 1.61 g/cm^3 as a function of total simulation time t_{max} at 300 K for a time step Δt of 0.1 fs, maximum correlation time averaging window $\Delta\tau_{max}$ between 4 and 8 ps, and system length L of 27.8 Å.

Moreover, numerical convergence of the results in terms of system size was evaluated by considering system lengths ranging from 17.8 to 28.4 Å for a density of 3.54 g/cm^3. Figure 6 plots the thermal conductivity k_c of hydrogen-free nonporous amorphous carbon with density 3.54 g/cm^3 as a function of system length L at 300 K obtained for a time step Δt of 0.1 fs, a maximum correlation time τ_{max} averaging window between 4 and 8 ps, and a total simulation time t_{max} of 4.5 ns. It indicates that a simulation cell length of 21.3 Å (i.e., 6×6×6 unit cells and 1728 carbon atoms) was sufficient to obtain values of thermal conductivity that were independent of system length. Thus, all systems presented in this study consisted of

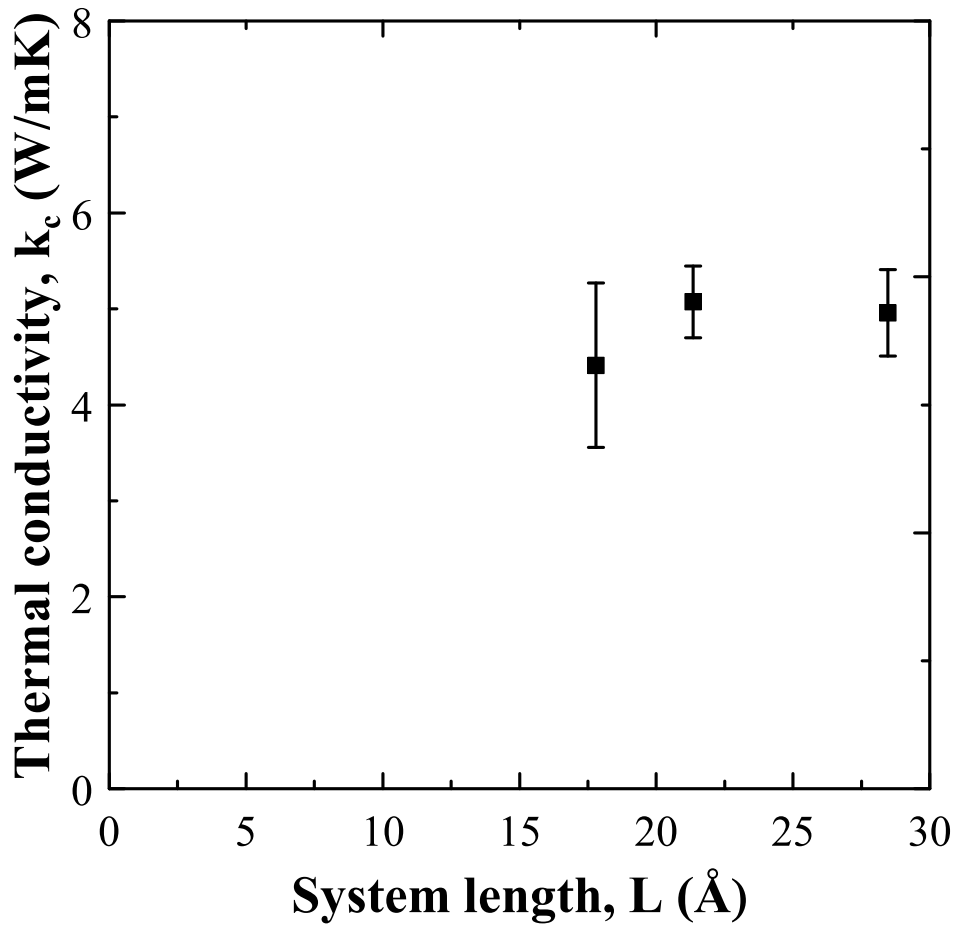

Figure 6: Thermal conductivity k_c of hydrogen-free nonporous amorphous carbon with density ρ_c of 3.54 g/cm^3 as a function of system length L at 300 K for a time step Δt of 0.1 fs, maximum correlation time averaging window $\Delta\tau_{max}$ between 4 and 8 ps, and total simulation time t_{max} of 4.5 ns.

6×6×6 unit cells. For a density of 3.54 g/cm^3 this corresponded to a system length of 21.3 Å. When the 6×6×6 unit cells were isotropically expanded to produce systems with lower densities of 2.66, 2.05, and 1.61 g/cm^3, the resulting system lengths were 23.6, 25.7, and 27.8 Å, respectively.

3.2 Nanoporous amorphous carbon

In order to simulate nanoporous amorphous carbon a spherical pore was introduced into the dense amorphous carbon system by removing carbon atoms located in a spherical region

around the center of the simulation box. The pore diameter d_p ranged from 9.76 to 26.0 Å in diameter corresponding to porosity f_v varying from 5 to 40% for system length L of 21.3 to 32.0 Å. For the pore size considered, Kn was very large and k_d was approximately zero according to Equation (10). Thus, the pores were simulated as empty. The system was equilibrated at 300 K using the NVE ensemble. Then, the effective thermal conductivity k_{eff} was estimated using the Green-Kubo relation for the NVT ensemble. For all structures considered, a numerically converged solution was obtained with a the time step Δt of 0.1 fs and a maximum correlation time τ_{max} averaging window between 4 and 8 ps. In addition, the total simulation time t_{max} increased from 4.5 to 6.5 ns as porosity increased from 0 to 40%.

4 Results and discussion

4.1 Hydrogen-free nonporous amorphous carbon

The radial distribution function of atoms represents the number of atoms in a spherical shell located at a given distance from a reference atom. It can be used to compare the atomic structures of systems. Moreover, it can be determined experimentally using neutron scattering [2] or obtained numerically using MD simulations [3]. The radial distribution function $g(r)$ is defined such that the average number of atoms $n(r)$ in a spherical shell centered at distance r from a reference particle and with thickness dr and is expressed as [83]

$$n(r)\mathrm{d}r = 4\pi n_0 g(r) r^2 \mathrm{d}r \tag{17}$$

where n_0 is the number density of atoms (in $\#/\mathrm{m}^3$). Generally, the reduced radial distribution function $G(r)$ is reported rather than the radial distribution function and is defined as [3]

$$G(r) = 4\pi r \rho [g(r) - 1] \tag{18}$$

where ρ is the density in $\mathrm{g/cm}^3$. According to Equation (8), the density is related to the number density of atoms by the molar mass M and Avogadro's constant N_A. Physically,

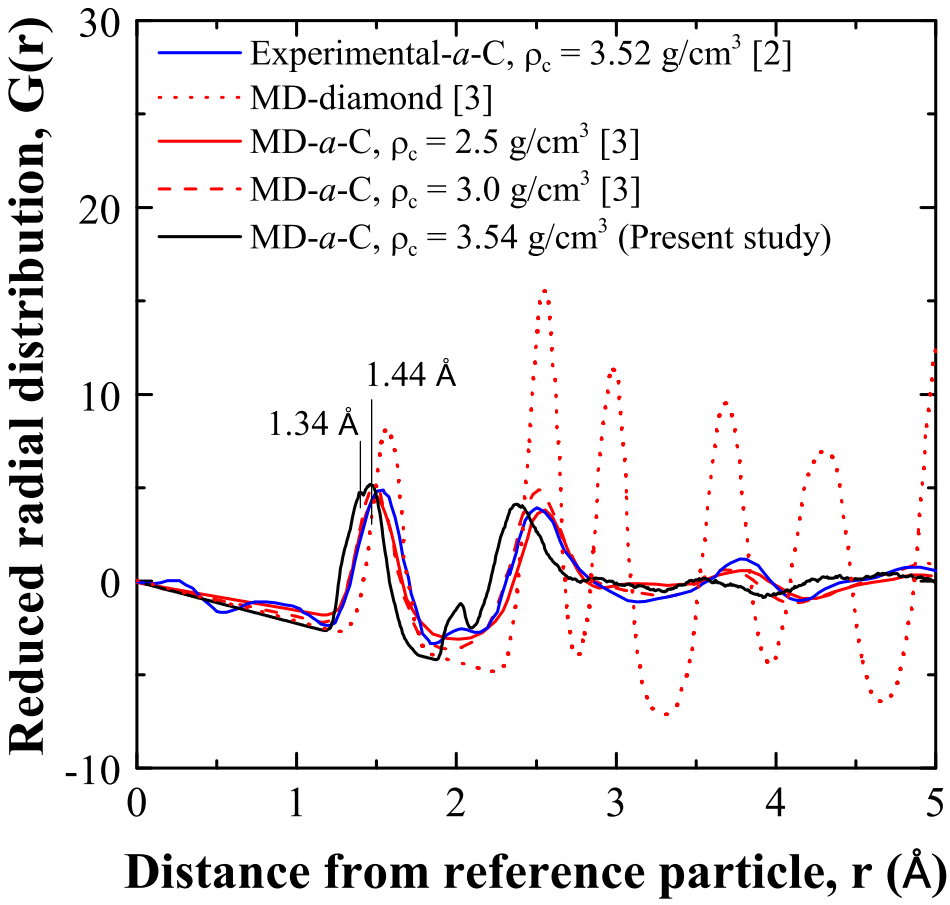

Figure 7: Comparison of the reduced radial distribution function $G(r)$ obtained in the present study for hydrogen-free nonporous amorphous carbon (ρ_c = 3.54 g/cm^3) and for (i) experimentally measured amorphous carbon [2], (ii) diamond simulated using MD simulations [3], and (iii) amorphous carbon obtained using MD simulations [3] all at 300 K.

positive values of the reduced radial distribution function $G(r)$ represent atom densities greater than the average, whereas negative values represent atom densities lower than the average [84]. The peaks observed in $G(r)$ represent distinct distances at which neighboring atoms are found, in other words, the typical bond lengths of the system [85]. Gaskell et al. [2] experimentally measured $G(r)$ for tetrahedral amorphous diamondlike carbon using neutron scattering. In addition, Stephan *et al.* [3] used the Tersoff potential to model C-C interactions for diamond and amorphous carbon with density of 2.5 and 3.0 g/cm^3 to predict the reduced radial distribution function $G(r)$ at 300 K.

Figure 7 compares the reduced carbon-carbon radial distribution function $G(r)$ at 300 K obtained in the present study for hydrogen-free nonporous amorphous carbon ($\rho_c = 3.54$ g/cm^3) with those of amorphous carbon of various density determined experimentally [2] and of diamond and amorphous carbon determined by MD simulations [3]. It indicates that the results obtained in the present study agreed well with those reported in the literature [2,3]. As expected, the reduced radial distribution function of amorphous carbon was significantly different from that of diamond. The first peak in $G(r)$ of amorphous carbon was split into two local maxima. The first was centered around 1.34 Å corresponding to the length of a C-C double bond [85]. The second local maxima was centered around 1.44 Å which is somewhat smaller than the C-C single bond length of 1.54 Å [85]. Nevertheless, this second peak in $G(r)$ likely corresponded to sp^3 hybridized atoms. Note that the splitting of the first was peak was previously observed in the radial distribution function of titrated amorphous carbon predicted using MD simulations [85]. The hybridization of the carbon atoms was determined by counting the number of neighboring atoms within 1.7 Å of the reference carbon atom [86]. The local minima at 1.4 Å between the first two peaks represents a relatively low density of neighboring atoms at this distance. Thus, the distance of 1.4 Å was used as the cutoff distance to differentiate between sp^3 and sp^2 hybridizations.

Table 2 reports the density ρ_c and thermal conductivity k_c at 300 K of hydrogen-free nonporous amorphous carbon simulated using MD simulations.

Table 2: Summary of the density ρ_c and thermal conductivity k_c of hydrogen-free nonporous amorphous carbon at 300 K predicted using MD simulations.

	ρ_c	k_c
	(g/cm^3)	**(W/m·K)**
Hydrogen-free nonporous	3.54	5.07
	2.66	2.97
	2.05	2.46
	1.61	1.92

Figure 8 compares the thermal conductivity k_c of hydrogen-free nonporous amorphous carbon at 300 K as a function of density ρ_c of the dense amorphous carbon predicted in the present study with results previously obtained experimentally [6, 7] and by other MD simulation studies [8, 9]. The amorphization procedure described previously was used to generate the amorphous carbon precursors for nanoporous carbon. All MD simulations predicted somewhat larger thermal conductivity than recent experimental measurements [6, 7]. The thermal conductivity of amorphous carbon with density of 3.54 g/cm^3 was also predicted using the Tersoff potential [52]. However, it was somewhat larger than that predicted using the AIREBO potential [4]. Thus, the latter was used for the remaining simulations. Note that the experimentally measured thermal conductivity reported by Morath *et al.* [15] for hydrogen-free nonporous amorphous carbon was significantly larger than those reported by other experimental studies [6, 7] and obtained by MD simulations [8, 9]. As previously discussed, the measurement method relied on estimates of material properties which may not be known reliably. Thus, this data was not shown. Finally, MD simulations using the AIREBO potential predicted slightly larger thermal conductivities than those using EDIP [9] and the REBO potential [8]. Overall, all MD simulations were in relatively good agreement with one another regardless of the different interatomic potential considered. All of them overpredicted the experimental measurements [6, 7].

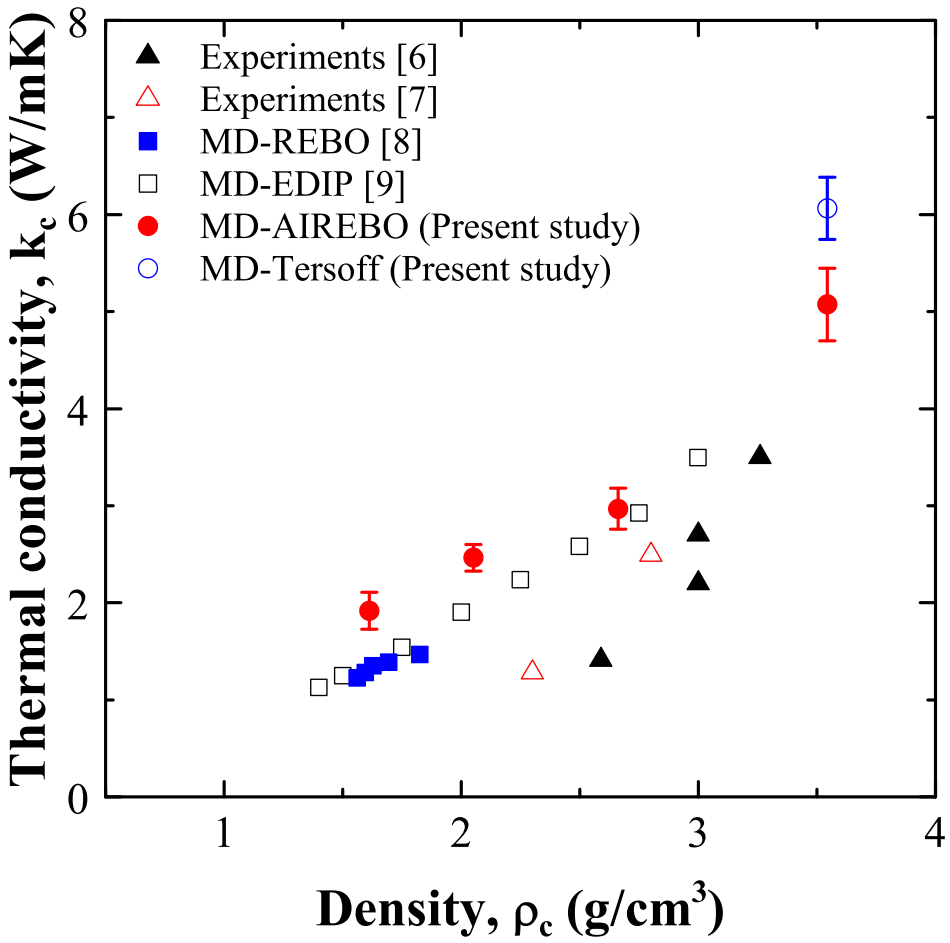

Figure 8: Comparison of the thermal conductivity k_c of hydrogen-free nonporous amorphous carbon at room temperature as a function of density ρ_c obtained (i) in the present study using the AIREBO [4] and Tersoff [5] potentials, (ii) experimentally [6, 7], and (iii) by previous MD simulations using the REBO [8] and EDIP [9] potentials.

4.2 Nanoporous amorphous carbon

4.2.1 Effect of pore diameter

Table 3: Summary of the system length L, the spherical pore diameter d_p, and the effective thermal conductivity k_{eff} of nanoporous amorphous carbon at 300 K for various porosity f_v and corresponding effective density ρ_{eff} predicted using MD simulations.

f_v (%)	ρ_{eff} (g/cm^3)	L (Å)	d_p (Å)	k_{eff} (W/m·K)
10	3.19	21.3	12.3	4.26 ± 0.41
		24.9	14.3	4.23 ± 0.34
		28.5	16.4	4.32 ± 0.28
		32.0	18.4	3.84 ± 0.24
25	2.67	21.3	16.7	3.12 ± 0.29
		24.9	19.5	3.05 ± 0.24
		28.5	22.2	2.82 ± 0.19
		32.0	25.0	3.06 ± 0.40
40	2.12	21.3	19.5	2.22 ± 0.05
		24.9	22.8	2.22 ± 0.12
		28.5	26.0	2.04 ± 0.17

Table 3 summarizes the different nanoporous amorphous carbon simulated to investigate the effect of the pore diameter d_p on the effective thermal conductivity k_{eff}. The latter was predicted at 300 K for effective densities ρ_{eff} of 3.19, 2.67, and 2.12 g/cm^3 corresponding to porosities f_v of 10, 25, and 40%, respectively. All of these systems were derived from a hydrogen-free nonporous amorphous carbon precursor having a density ρ_c of 3.54 g/cm^3. The system length was varied from 21.3 to 32.0 Å and the pore diameter was adjusted between 12.3 and 26.0 Å to achieve the desired porosity. Note that the effective density ρ_{eff} was computed from the mass and volume of the structure. This effective density agreed with that

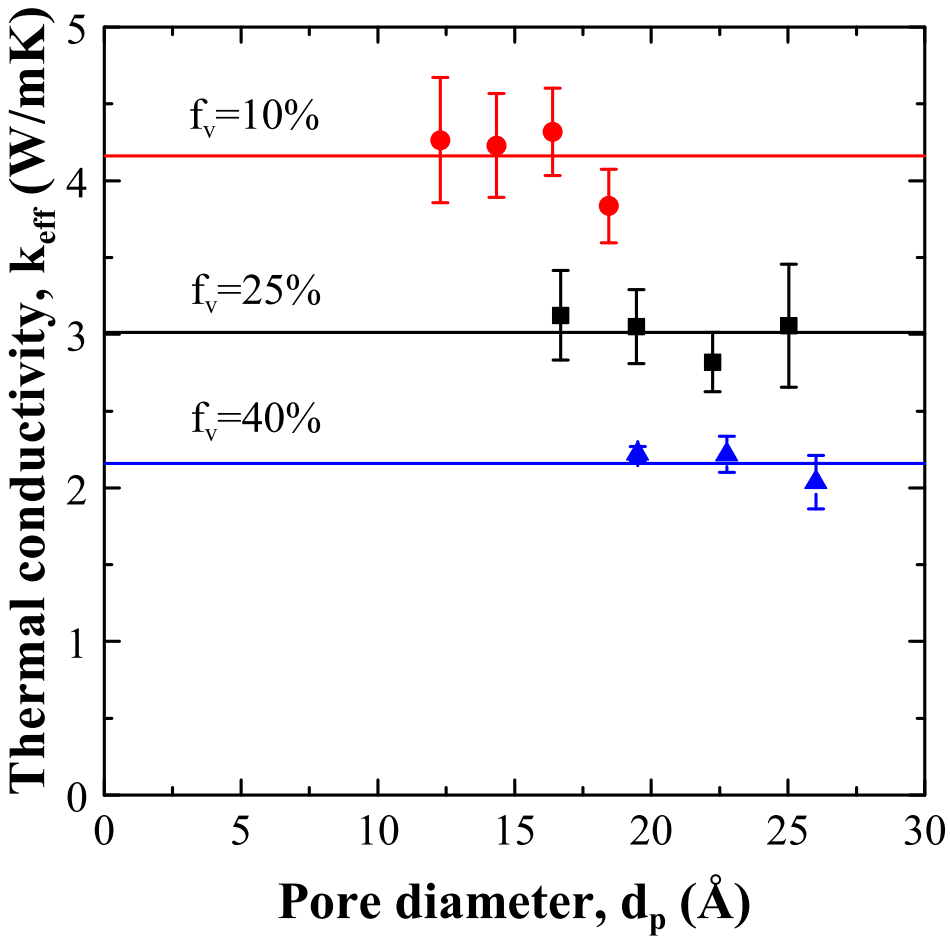

Figure 9: Effective thermal conductivity k_{eff} of nanoporous amorphous carbon at 300 K as a function of pore diameter d_p for porosity f_v of 10, 25, and 40%.

computed using Equation (16) within less than 1%. The slight difference in effective density comes from the finite size of the atoms that were removed to create the pore. Therefore, the pore was not perfectly spherical, as shown in Figure 2c. However, the pore was assumed to be perfectly spherical when determining the pore diameter corresponding to a given porosity.

Figure 9 shows the effective thermal conductivity k_{eff} of nanoporous amorphous carbon as a function of pore diameters d_p for different values of porosity f_v. It indicates that the effective thermal conductivity decreased with increasing porosity. More importantly, it establishes that the effective thermal conductivity was independent of pore diameter for any given porosity. Note that similar conclusions were reached from MD simulations of

nanoporous silica (amorphous) [12].

4.2.2 Effect of porosity

Table 4 summarizes the characteristics of the nanoporous amorphous carbon systems simulated by MD simulations for four different initial matrix density ρ_c and corresponding to matrix thermal conductivity k_c. It also reports their effective thermal conductivity k_{eff} of nanoporous carbon and the ratio k_{eff}/k_c at 300 K for a wide range of porosity f_v, and corresponding effective density ρ_{eff}. As in the previous section, the effective density ρ_{eff} was computed from the mass and volume of the structure. Note that the effective density computed using this method agreed with that computed using Equation (16) within 1%. The uncertainty reported for k_c and k_{eff} corresponded to a 95% confidence interval from seven independent simulations. Additionally, the uncertainty for k_{eff}/k_c was determined through error propagation.

Figure 10a plots the predicted effective thermal conductivity k_{eff} of nanoporous amorphous carbon at 300 K as a function of porosity f_v ranging from 0 to 40% for four different initial continuous phase densities ρ_c varying between 1.61 and 3.54 g/cm^3. For each initial continuous phase density, the porosity was varied by adjusting the pore diameter, and keeping the system length constant, to correspond with a given porosity. As expected, for a given continuous phase density ρ_c, the effective thermal conductivity decreased with increasing porosity. Figure 10b shows the ratio k_{eff}/k_c as a function of porosity f_v for the four different initial densities ρ_c considered where k_c represented the thermal conductivity of the nonporous amorphous carbon (f_v=0%). The scaled data tend to overlap, within numerical uncertainty, indicating a self-similar behavior in the form

$$k_{eff} = k_c \psi(f_v) \tag{19}$$

where $\psi(f_v)$ is a function of porosity only. Figure 10b also plots the ratio k_{eff}/k_c predicted by the parallel, Maxwell Garnett, coherent potential, and percolation models given by Equations (11), (12), (14), and (15), respectively. It indicates that, for porosity ranging from 0 to 40%, both the Maxwell Garnett model and the coherent potential model agreed well with the predictions from MD simulations. The average relative errors between predictions by the Maxwell Garnett model and the coherent potential model and the predictions from

Table 4: Summary of the effective density ρ_{eff}, effective thermal conductivity k_{eff}, and ratio k_{eff}/k_c at 300 K of nanoporous amorphous carbon for various porosity f_v predicted using MD simulations.

ρ_c (g/cm^3)	k_c (W/m·K)	f_v (%)	ρ_{eff} (g/cm^3)	k_{eff} (W/m·K)	k_{eff}/k_c
3.54	5.07 ± 0.37	5	3.38	4.56 ± 0.45	0.90 ± 0.11
		10	3.19	4.26 ± 0.41	0.84 ± 0.10
		15	3.00	3.58 ± 0.30	0.71 ± 0.08
		20	2.83	3.24 ± 0.22	0.64 ± 0.06
		25	2.67	3.12 ± 0.29	0.62 ± 0.07
		30	2.48	2.57 ± 0.06	0.51 ± 0.04
		35	2.30	2.37 ± 0.25	0.47 ± 0.06
		40	2.12	2.22 ± 0.05	0.44 ± 0.03
2.66	2.97 ± 0.21	5	2.53	2.69 ± 0.18	0.91 ± 0.09
		10	2.39	2.56 ± 0.28	0.86 ± 0.11
		15	2.26	2.29 ± 0.17	0.77 ± 0.08
		20	2.13	2.17 ± 0.12	0.73 ± 0.07
		25	2.01	1.90 ± 0.16	0.64 ± 0.07
		30	1.87	1.78 ± 0.15	0.60 ± 0.07
		35	1.73	1.61 ± 0.11	0.54 ± 0.05
		40	1.59	1.56 ± 0.25	0.53 ± 0.09
2.05	2.46 ± 0.14	5	1.95	2.05 ± 0.10	0.83 ± 0.06
		10	1.84	1.97 ± 0.18	0.80 ± 0.09
		15	1.73	1.88 ± 0.15	0.76 ± 0.08
		20	1.64	1.74 ± 0.17	0.70 ± 0.08
		25	1.54	1.61 ± 0.12	0.65 ± 0.06
		30	1.42	1.40 ± 0.16	0.57 ± 0.07
		35	1.33	1.27 ± 0.11	0.52 ± 0.05
		40	1.24	1.19 ± 0.07	0.48 ± 0.04
1.61	1.92 ± 0.19	5	1.53	1.61 ± 0.11	0.84 ± 0.10
		10	1.45	1.63 ± 0.12	0.85 ± 0.11
		15	1.39	1.44 ± 0.11	0.75 ± 0.09
		20	1.30	1.30 ± 0.10	0.68 ± 0.08
		25	1.22	1.29 ± 0.25	0.67 ± 0.15
		30	1.13	1.21 ± 0.10	0.63 ± 0.08
		35	1.06	1.21 ± 0.15	0.63 ± 0.10
		40	0.97	1.13 ± 0.06	0.59 ± 0.06

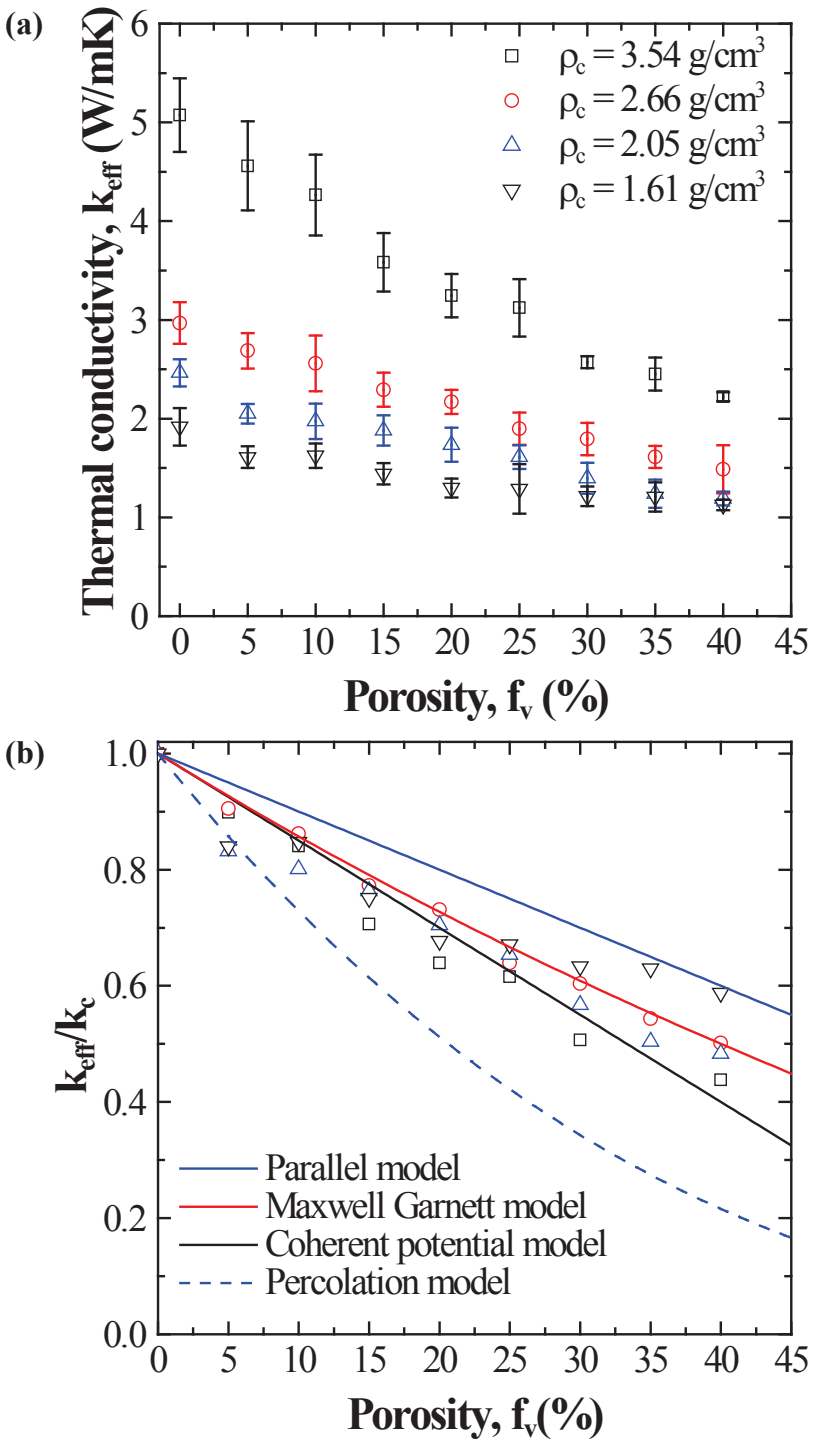

Figure 10: (a) Effective thermal conductivity k_{eff} and (b) ratio of k_{eff}/k_c as a function of porosity f_v at 300 K for nanoporous amorphous carbon. The solid blue, solid red, solid black, and dashed blue lines correspond to predictions by the parallel, Maxwell Garnett, coherent potential, and percolation models, given by Equations (11), (12), and (14), and (15) respectively.

MD simulations were 6 and 7%, respectively. Moreover, the relative error increased with increasing porosity. It reached up to 20% and 32% for f_v=40% for the Maxwell Garnett and the coherent potential models, respectively. Overall, the Maxwell Garnett model was somewhat better than the coherent potential model at capturing the evolution of the ratio k_{eff}/k_c as a function of porosity f_v.

4.2.3 Effective density

As previously reviewed, the effective thermal conductivity of carbon aerogels has often been reported as a function of effective density ρ_{eff} rather than porosity f_v [10, 11]. Figure 11 plots the effective thermal conductivity k_{eff} of nanoporous amorphous carbon at 300 K, obtained from MD simulations, as a function of the effective density, computed from the mass and volume of the structure, and ranging from 1.22 to 3.54 g/cm^3. It also shows the experimentally measured thermal conductivity at room temperature of carbon aerogels pyrolized at 1050°C [10,11]. The latter was proportional to $\rho_{eff}^{1.5}$ [10] and $\rho_{eff}^{2.2}$ [11] for effective density ranging from 0.06 to 0.65 g/cm^3 and 0.381 to 0.984 g/cm^3. Similarly, the effective thermal conductivity k_{eff} of nanoporous amorphous carbon obtained in this study could be related to the effective density ρ_{eff} by a power-type of law given by

$$k_{eff} = 0.98\rho_{eff}^{1.2} \tag{20}$$

where the coefficient 0.98 and power 1.2 were obtained by least squares fitting. The associated coefficient of determination R^2 was equal to 0.95. Figure 11 also indicates that Equation (20) could also be used as a first-order estimate of the effective thermal conductivity of carbon aerogels pyrolized at 1050°C as a function of effective density. Note however, that the pyrolysis temperature strongly affected the effective thermal conductivity of carbon aerogels by curing defects in the carbon matrix while the effective density remained relatively constant [67]. Defects in aerogels, including micro-cracks, micro-porosity, and impurities, decrease the phonon mean free path and the effective thermal conductivity [13]. These defects were not produced in the nanoporous carbon structures investigated in the present study. Defects in the micro-scale would require larger nanoporous carbon systems than those simulated presently. However, the systems modeled in the present study were already computationally expensive and modeling significantly larger systems would not be feasible with the available resources.

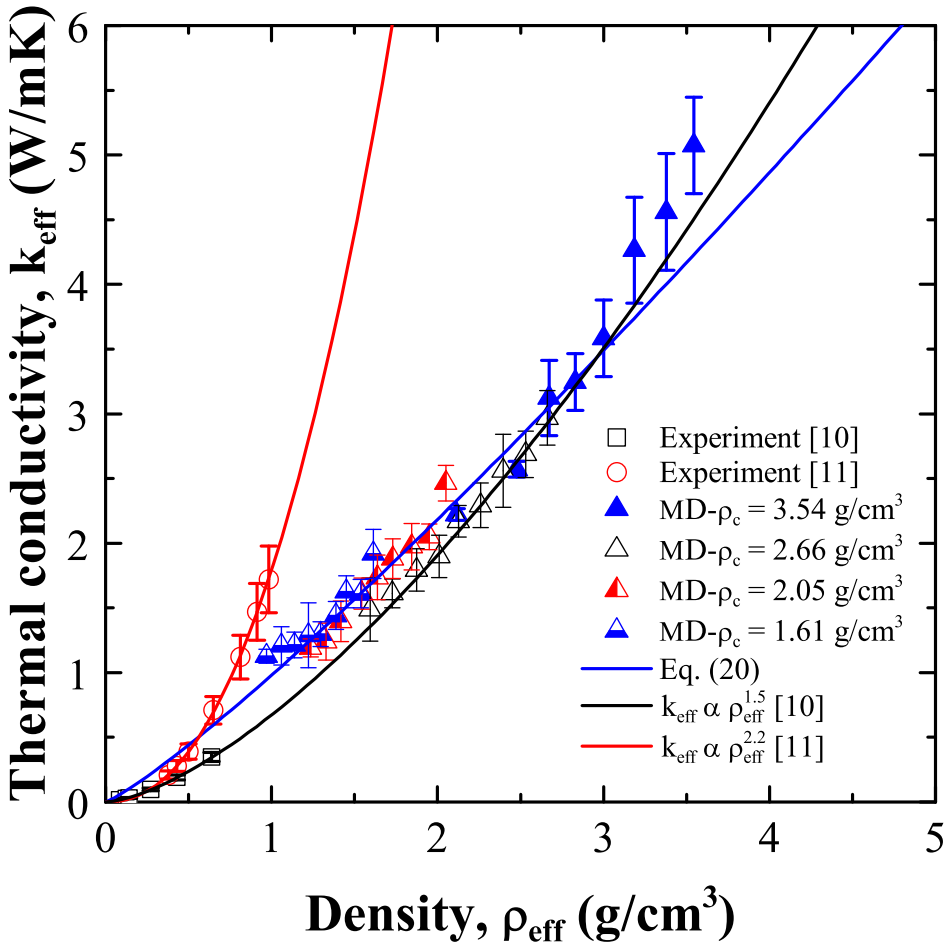

Figure 11: Effective thermal conductivity k_{eff} of nanoporous amorphous carbon at 300 K as a function of effective density ρ_{eff} obtained using MD simulations with the associated best fit power law. Experimental results and the associated power law relations for carbon aerogels are also included [10, 11].

4.2.4 Comparison with nanoporous silica

As previously discussed, Coquil *et al.* [12] predicted the effective thermal conductivity k_{eff} of nanoporous silica at 300 K using MD simulations for porosity f_v ranging from 10 to 35% corresponding to effective density ρ_{eff} between 1.44 and 2.22 g/cm^3. The authors showed that k_{eff} could be modeled by the coherent potential approximation. Ng *et al.* [13] predicted the effective thermal conductivity of silica aerogels at 300 K using MD simulations for effective density ranging from 0.32 to 0.99 g/cm^3. Note that both of these studies employed non-equilibrium MD simulations and the so-called BKS potential [12,13]. Furthermore, Jain

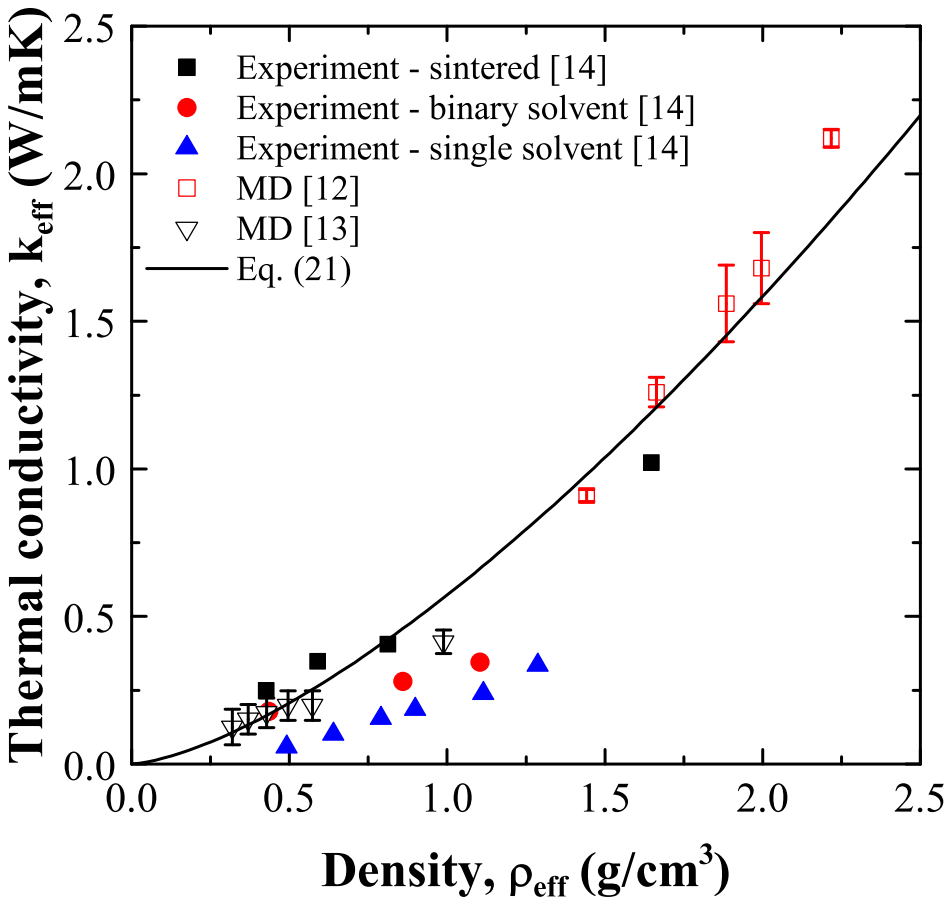

Figure 12: Comparison of the effective thermal conductivity k_{eff} of nanoporous silica at 300 K as a function of effective density ρ_{eff} obtained using MD simulations [12, 13] and experimentally [14]. The solid line represents the best fit power law relation for the MD simulations data.

et al. [14] measured the effective thermal conductivity of silica aerogels at room temperature for effective density ranging from 0.4 to 1.6 g/cm^3. These aerogels were synthesized using either the sintering, binary solvent, or single solvent method [14]. Here also, the effective thermal conductivity of low porosity nanoporous silica could be related to the effective density. In fact, Ng *et al.* [13] determined that the effective thermal conductivity k_{eff} of silica aerogels predicted from MD simulations was proportional to $\rho_{eff}^{1.01}$. Similarly, Jain *et al.* [14] experimentally determined that the effective thermal conductivity was dependent on the aerogel synthesis method and related to effective density by the power law $k_{eff} \propto \rho_{eff}^{n}$. The coefficient n was equal to 1.04, 1.00, and 1.65 for aerogels synthesized by the sintering,

binary solvent, and single solvent methods, respectively.

Figure 12 compares the effective thermal conductivity of nanoporous silica predicted using MD simulations [12, 13] with that measured experimentally [14] as a function of effective density at room temperature. It indicates that the effective thermal conductivity of nanoporous silica predicted from MD simulations [12, 13] could be related to the effective density according to a power law expressed as

$$k_{eff} = 0.57\rho_{eff}^{1.5}. \tag{21}$$

This was valid for effective density ρ_{eff} ranging from 0.32 to 2.22 g/cm^3 encompassing silica aerogels [13] and low porosity (10-35%) nanoporous silica [12] predicted using MD simulations with a coefficient of determination R^2 of 0.98. Furthermore, the effective thermal conductivity predicted using MD simulations was in good agreement with measurements for silica aerogels made by the sintering method. On the contrary, they overestimated experimental measurements for silica aerogels made by single and binary solvent methods. As noted previously, micro-scale defects were responsible for lowering the effective thermal conductivity of the aerogels [13]. This can be attributed to the fact that these defects were not accounted for in the MD simulations and that sintering removed many of the defects in the silica aerogel [12, 13]. This also explains the larger effective thermal conductivity predicted by the MD simulation studies [12, 13] compared to those measured experimentally [14].

5 Conclusions

The present study investigated the thermal conductivity of nanoporous amorphous carbon at 300 K using MD simulations and the Green-Kubo method. The AIREBO potential was used to model C-C atomic interactions. First, the simulation method was validated by comparing the predicted thermal conductivity of hydrogen-free nonporous amorphous carbon with experimental and MD simulation results reported in the literature [6–9, 16]. Then, nanoporous amorphous carbon was generated by introducing a spherical pore into a hydrogen-free nonporous structure. The effective thermal conductivity of nanoporous amorphous carbon at 300 K was computed for pore diameter, porosity, and effective density ranging from 9.76 to 21.7 Å, 5 to 40%, and 1.22 to 3.38 g/cm^3, respectively. The effective thermal conductivity was found to be independent of pore diameter and dependent on porosity only. Addition-

ally, the ratio k_{eff}/k_c was in good agreement with the Maxwell Garnett model for porosity ranging from 0 to 40%. Alternatively, a power law relation between the effective thermal conductivity and the effective density of nanoporous carbon was developed. This relation could also provide a first-order estimate of the effective thermal conductivity of carbon aerogels. Furthermore, the effective thermal conductivity of silica aerogels [13] and low porosity (10-35%) nanoporous silica [12] obtained in previous studies using MD simulations was also found to be related to the effective density by a power law.

Appendices

A LAMMPS input script for generating amorphous carbon and computing the thermal conductivity using the Green-Kubo method

```
#####################################################
# Initialization ####################################
#####################################################

units metal                                     # Type of units used

# Variables #################################################

variable T1 equal 15000                         # Kelvin
variable T2 equal 300                           # Kelvin
variable V equal vol                            # Volume
variable dt equal 0.0001                        # Time step
variable p equal 10000                          # Correlation length
variable s equal 10                             # Sample interval
variable d equal $p*$s                          # Dump interval

# Setup #####################################################

dimension 3                                     # Defines a 3D simulation
boundary p p p                                  # Defines periodic boundary conditions
atom_style charge                               # Defines atom types to be charge
lattice diamond 3.57                            # Defines a diamond lattice with unit length
                                                # 3.57 A
region box block 0 6 0 6 0 6                    # Defines a 3D block region called "box" that
                                                # is made up of the unit cell repeated 6 times
                                                # in the x-, y-, and z-directions
create_box 1 box                                # Creates the simulation box defined by the
                                                # previous region command
create_atoms 1 box                              # Creates the atoms within the simulation box
                                                # according to the defined lattice
mass 1 12.0107                                  # Defines the molar mass of atom type 1
group carbonatoms type 1                        # Assigns the name carbonators to atom type 1

# Interatomic potential #####################################

pair_style airebo 3.0                           # Defines the pair style for the atomic potential
                                                # interactions to be AIREBO
pair_coeff * * CH.airebo C                      # Defines the interactions to be between carbon
                                                # atoms
neighbor 2.0 bin                                # The neighbor distance is given by the potential
                                                # cutoff + 2A
neigh_modify delay 10 every 1 check yes         # Rebuilds the neighbor every 10 time steps only
                                                # if an atom has moved at least half the
                                                # skin distance

#####################################################
# Equilibration and thermalization ##################
#####################################################

fix 1 all box/relax iso 0.0 vmax 0.001          # Zero pressure condition applied to external
                                                # bounds of simulation box
min_modify line quadratic                       # Applies a quadratic line search algorithm for
                                                # the energy minimization
minimize 0.000001 0.00000001 10000 100000       # Iteratively adjusts atom coordinates to
                                                # minimize the energy of the system
unfix 1                                         # Stops the zero pressure condition
timestep ${dt}                                  # Sets the time step to 0.1 fs
thermo 500                                      # Outputs thermodynamic data every 500 time steps
reset_timestep 0                                # Resets the time step counter to zero
dump 1 carbonatoms xyz 1000 Melt.1.xyz          # Outputs coordinates to Melt.1.xyz
```

```
dump 2 all atom 1000 Melt.1.lammpstrj           # Outputs coordinates to Melt.1.lammpstrj
velocity all create ${T1} 102486 mom yes &      # Randomly sets initial velocity to correspond
rot yes dist gaussian                           # with 15,000 K
fix NVT all nvt temp ${T1} ${T2} 0.09 drag 0.4  # Integrates atomic positions using the NVT
                                                # ensemble as temperature is decreased from
                                                # 15,000 K to 300 K
run 80000                                       # Runs the integration in NVT for 80,000 time
                                                # steps
unfix NVT                                       # Ends the NVT integration
fix NVT2 all nvt temp ${T2} ${T2} 0.09 drag 0.4 # Integrates atomic positions using the NVT
                                                # ensemble for a temperature of 300 K
run 100000
undump 1                                        # Ends the output of coordinates to Melt.1.xyz
undump 2                                        # Ends the output of coordinates to
                                                # Melt.1.lammpstrj
write_restart endNVT.restart                    # Writes a restart file to endNVT.restart
restart $d Melt.*.restart                       # Writes a restart file every 100,000 time steps
dump 3 carbonatoms xyz 10000 Melt.2.xyz         # Outputs coordinates to Melt.2.xyz
dump 4 all atom 10000 Melt.2.lammpstrj          # Outputs coordinates to Melt.2.lammpstrj

#####################################################
# Green Kubo Method #################################
#####################################################

compute myKE all ke/atom                        # Computes the kinetic energy per atom
compute myPE all pe/atom                        # Computes the potential energy per atom
compute myStress all stress/atom virial         # Computes the stresses per atom excluding
                                                # kinetic energy contributions
compute flux all heat/flux myKE myPE myStress   # Computes the heat flux vector
variable Jx equal c_flux[1]/vol
variable Jy equal c_flux[2]/vol
variable Jz equal c_flux[3]/vol
fix JJ all ave/correlate $s $p $d c_flux[1] &   # Calculates the heat current autocorrelation
c_flux[2] c_flux[3] type auto file &            # function
J0Jt_Melt.dat ave running
thermo $d                                       # Outputs thermodynamic data every 100,000 time
                                                # steps
thermo_style custom step temp v_Jx v_Jy v_Jz    # Defines the thermodynamic data to output
run 45000000                                    # Runs the Green Kubo method for 45,000,000 time
                                                # steps
write_restart end.restart                       # Writes a restart file end.restart
```

B LAMMPS input script for generating amorphous carbon with lower density and computing the thermal conductivity using the Green-Kubo method

```
#####################################################
# Initialization ####################################
#####################################################

read_restart endNVT.restart                       # Open file created by the script generating
                                                  # amorphous carbon

# Variables #########################################

variable T2 equal 300                             # Kelvin
variable V equal vol                              # Volume
variable dt equal 0.0001                          # Time step
variable p equal 10000                            # correlation length
variable s equal 10                               # sample interval
variable d equal $p*$s                            # dump interval

# Interatomic potential #############################

pair_style airebo 3.0                             # Defines the pair style for the atomic potential
                                                  # interactions to be AIREBO
pair_coeff * * CH.airebo C                        # Defines the interactions to be between carbon
                                                  # atoms
neighbor 2.0 bin                                  # The neighbor distance is given by the potential
                                                  # cutoff + 2A
neigh_modify delay 10 every 1 check yes           # Rebuilds the neighbor every 10 time steps only
                                                  # if an atom has moved at least half the
                                                  # skin distance
change_box all x scale 1.3 y scale 1.3 &          # Scale atom coordinates by 1.3 times in all
z scale 1.3 remap                                 # directions

print $V                                          # Print new volume

#####################################################
# Equilibration ####################
#####################################################

timestep ${dt}
thermo 1000                                       # Outputs thermodynamic data every 1000 time steps
fix NVT all nvt temp ${T2} ${T2} 0.09 drag 0.4    # Integrates atomic positions using the NVT
                                                  # ensemble for a temperature of 300 K
run 500000                                        # Runs the integration in NVT for 500,000 time
write_restart D30endNVT.restart                   # Writes a restart file D30endNVT.restart
restart $d D30.*.restart                          # Writes a restart file D30.*.restart every d time
                                                  # steps where the * is filled in by time step at
                                                  # which the file is written

#####################################################
# Green Kubo Method #################################
#####################################################

compute myKE all ke/atom                          # Computes the kinetic energy per atom
compute myPE all pe/atom                          # Computes the potential energy per atom
compute myStress all stress/atom virial           # Computes the stresses per atom excluding
                                                  # kinetic energy contributions
compute flux all heat/flux myKE myPE myStress     # Computes the heat flux vector
variable Jx equal c_flux[1]/vol
variable Jy equal c_flux[2]/vol
variable Jz equal c_flux[3]/vol
fix JJ all ave/correlate $s $p $d c_flux[1] &     # Calculates the heat current autocorrelation
c_flux[2] c_flux[3] type auto file &              # function
J0Jt_D30.dat ave running
thermo $d                                         # Outputs thermodynamic data every 100,000 time
                                                  # steps
thermo_style custom step temp v_Jx v_Jy v_Jz      # Defines the thermodynamic data to output
```

```
run 45000000                                # Runs the Green Kubo method for 45,000,000 time
                                            # steps
write_restart D30end.restart                # Writes a restart file D30end.restart
```

C LAMMPS input script for generating porous amorphous carbon and computing the thermal conductivity using the Green-Kubo method

```
#####################################################
# Initialization ####################################
#####################################################

read_restart endNVT.restart                       # Open file created by the script generating
                                                  # amorphous carbon

# Variables #########################################

variable T2 equal 300                             # Kelvin
variable V equal vol                              # Volume
variable dt equal 0.0001                          # Time step
variable p equal 10000                            # correlation length
variable s equal 10                               # sample interval
variable d equal $p*$s                            # dump interval

# Setup #############################################

lattice diamond 3.57 region pore1 sphere 3 3 3 & # Define spherical region by specifying the center
2.613872345                                       # coordinates and radius.  Here, radius is for 30%
                                                  # porosity
delete_atoms region pore1                         # Remove atoms within a spherical region
# Interatomic potential #############################

pair_style airebo 3.0                             # Defines the pair style for the atomic potential
                                                  # interactions to be AIREBO
pair_coeff * * CH.airebo C                        # Defines the interactions to be between carbon
                                                  # atoms
neighbor 2.0 bin                                  # The neighbor distance is given by the potential
                                                  # cutoff + 2A
neigh_modify delay 10 every 1 check yes           # Rebuilds the neighbor every 10 time steps only
                                                  # if an atom has moved at least half the
                                                  # skin distance

#####################################################
# Equilibration ####################
#####################################################

timestep ${dt}
reset_timestep 0                                  # Resets the time step counter to zero
thermo 100000                                     # Outputs thermodynamic data every 100000 time steps
restart $d D0P3.*.restart                         # Writes a restart file D0P3.*.restart every d time
                                                  # steps where the * is filled in by time step at
                                                  # which the file is written
fix rescale all temp/rescale 1 ${T2} ${T2} 50 1   # Rescale temperature to 300 K if temperature is
                                                  # outside 300 K by 50 K
fix NVE all nve
run 100000                                        # Runs the integration in NVE for 100,000 time
unfix rescale                                     # Ends temperature rescaling
unfix NVE                                         # Ends NVE integration
fix NVT2 all nvt temp ${T2} ${T2} 0.09 drag 0.4
run 100000                                        # Runs the integration in NVT for 100,000 time
write_restart D0P3endNVT.restart                  # Writes a restart file D0P3endNVT.restart

#####################################################
# Green Kubo Method #################################
#####################################################

compute myKE all ke/atom                          # Computes the kinetic energy per atom
compute myPE all pe/atom                          # Computes the potential energy per atom
compute myStress all stress/atom virial           # Computes the stresses per atom excluding
                                                  # kinetic energy contributions
compute flux all heat/flux myKE myPE myStress     # Computes the heat flux vector
variable Jx equal c_flux[1]/vol
```

```
variable Jy equal c_flux[2]/vol
variable Jz equal c_flux[3]/vol
fix JJ all ave/correlate $s $p $d c_flux[1] &     # Calculates the heat current autocorrelation
c_flux[2] c_flux[3] type auto file &              # function
J0Jt_D0P3.dat ave running
thermo $d                                         # Outputs thermodynamic data every 100,000 time
                                                  # steps
thermo_style custom step temp v_Jx v_Jy v_Jz      # Defines the thermodynamic data to output
run 45000000                                      # Runs the Green Kubo method for 45,000,000 time
                                                  # steps
write_restart D0P3end.restart                     # Writes a restart file D0P3end.restart
```

6 References

[1] J. Robertson, "Diamond–like amorphous carbon", *Materials Science and Engineering: R: Reports*, vol. 37, no. 4–6, pp. 129–281, 2002.

[2] P. H. Gaskell, A. Saeed, P. Chieux, and D. R. McKenzie, "Neutron–scattering studies of the structure of highly tetrahedral amorphous diamondlike carbon", *Physical Review Letters*, vol. 67, pp. 1286–1289, 1991.

[3] U. Stephan and M. Haase, "A molecular dynamics study and the electronic properties of amorphous carbon using the Tersoff potential", *Journal of Physics: Condensed Matter*, vol. 5, pp. 9157–9168, 1993.

[4] S. J. Stuart, A. B. Tutein, and J. A. Harrison, "A reactive potential for hydrocarbons with intermolecular interactions", *The Journal of Chemical Physics*, vol. 112, no. 14, pp. 6472–6486, 2000.

[5] J. Tersoff, "Empirical interatomic potential for carbon, with applications to amorphous carbon", *Physical Review Letters*, vol. 61, no. 25, pp. 2879, 1988.

[6] M. Shamsa, W. L. Liu, A. A. Balandin, C. Casiraghi, W. I. Milne, and A. C. Ferrari, "Thermal conductivity of diamond–like carbon films", *Applied Physics Letters*, vol. 89, no. 16, pp. 161921, 2006.

[7] A. J. Bullen, K. E. O'Hara, D. G. Cahill, O. Monteiro, and A. von Keudell, "Thermal conductivity of amorphous carbon thin films", *Journal of Applied Physics*, vol. 88, no. 11, pp. 6317–6320, 2000.

[8] M. A. Makeev and D. Srivastava, "Thermal properties of char obtained by pyrolysis: A molecular dynamics simulation study", *Applied Physics Letters*, vol. 95, no. 18, pp. 181908, 2009.

[9] I. Suarez-Martinez and N. A. Marks, "Effect of microstructure on the thermal conductivity of disordered carbon", *Applied Physics Letters*, vol. 99, no. 3, pp. 033101, 2011.

[10] X. Lu, O. Nilsson, J. Fricke, and R. W. Pekala, "Thermal and electrical conductivity of monolithic carbon aerogels", *Journal of Applied Physics*, vol. 73, no. 2, pp. 581–584, 1993.

[11] V. Bock, O. Nilsson, J. Blumm, and J. Fricke, "Thermal properties of carbon aerogels", *Journal of Non-Crystalline Solids*, vol. 185, no. 3, pp. 233–239, 1995.

[12] T. Coquil, J. Fang, and L. Pilon, "Molecular dynamics study of the thermal conductivity of amorphous nanoporous silica", *International Journal of Heat and Mass Transfer*, vol. 54, no. 21–22, pp. 4540–4548, 2011.

[13] T. Y. Ng, J. J. Yeo, and Z. S. Liu, "A molecular dynamics study of the thermal conductivity of nanoporous silica aerogel, obtained through negative pressure rupturing", *Journal of Non–Crystalline Solids*, vol. 358, no. 11, pp. 1350–1355, 2012.

[14] A. Jain, S. Rogojevic, S. Ponoth, W. N. Gill, J. L. Plawsky, E. Simonyi, S.-T. Chen, and P. S. Ho, "Processing dependent thermal conductivity of nanoporous silica xerogel films", *Journal of Applied Physics*, vol. 91, no. 5, pp. 3275–3281, 2002.

[15] C. J. Morath, H. J. Maris, J. J. Cuomo, D. L. Pappas, A. Grill, V. V. Patel, J. P. Doyle, and K. L. Saenger, "Picosecond optical studies of amorphous diamond and diamondlike carbon: Thermal conductivity and longitudinal sound velocity", *Journal of Applied Physics*, vol. 76, no. 5, pp. 2636–2640, 1994.

[16] J. L. Arlein, S. E. M. Palaich, B. C. Daly, P. Subramonium, and G. A. Antonelli, "Optical pump–probe measurements of sound velocity and thermal conductivity of hydrogenated amorphous carbon films", *Journal of Applied Physics*, vol. 104, no. 3, pp. 033508, 2008.

[17] G. Salitra, A. Soffer, L. Eliad, Y. Cohen, and D. Aurbach, "Carbon electrodes for double–layer capacitors I. Relations between ion and pore dimensions", *Journal of The Electrochemical Society*, vol. 147, no. 7, pp. 2486–2493, 2000.

[18] A. Jänes, H. Kurig, and E. Lust, "Characterisation of activated nanoporous carbon for supercapacitor electrode materials", *Carbon*, vol. 45, no. 6, pp. 1226–1233, 2007.

[19] H. Gualous, H. Louahlia-Gualous, R. Gallay, and A. Miraoui, "Supercapacitor thermal modeling and characterization in transient state for industrial applications", *IEEE Transactions on Industry Applications*, vol. 45, no. 3, pp. 1035–1044, 2009.

[20] M. Al Sakka, H. Gualous, J. Van Mierlo, and H. Culcu, "Thermal modeling and heat management of supercapacitor modules for vehicle applications", *Journal of Power Sources*, vol. 194, no. 2, pp. 581–587, 2009.

[21] A. Nishino, "Capacitors: operating principles, current market and technical trends", *Journal of Power Sources*, vol. 60, no. 2, pp. 137–147, 1996.

[22] A. G. Pandolfo and A. F. Hollenkamp, "Carbon properties and their role in supercapacitors", *Journal of Power Sources*, vol. 157, no. 1, pp. 11–27, 2006.

[23] J. Zhao, C. Lai, Y. Dai, and J. Xie, "Pore structure control of mesoporous carbon as supercapacitor material", *Materials Letters*, vol. 61, no. 23-24, pp. 4639–4642, 2007.

[24] R. Kötz and M. Carlen, "Principles and applications of electrochemical capacitors", *Electrochimica Acta*, vol. 45, no. 15-16, pp. 2483–2498, 2000.

[25] S. R. S. Prabaharan, R. Vimala, and Z. Zainal, "Nanostructured mesoporous carbon as electrodes for supercapacitors", *Journal of Power Sources*, vol. 161, no. 1, pp. 730–736, 2006.

[26] R. K. Dash, G. Yushin, and Y. Gogotsi, "Synthesis, structure and porosity analysis of microporous and mesoporous carbon derived from zirconium carbide", *Microporous and Mesoporous Materials*, vol. 86, no. 13, pp. 50–57, 2005.

[27] R. W. Pekala, J. C. Farmer, C. T. Alviso, T. D. Tran, S. T. Mayer, J. M. Miller, and B. Dunn, "Carbon aerogels for electrochemical applications", *Journal of Non–Crystalline Solids*, vol. 225, pp. 74–80, 1998.

[28] A. d'Entremont and L. Pilon, "First-principles thermal modeling of electric double layer capacitors under constant-current cycling", *Journal of Power Sources*, vol. 246, pp. 887–898, 2014.

[29] J. R. Miller, "Electrochemical capacitor thermal management issues at high-rate cycling", *Electrochimica Acta*, vol. 52, no. 4, pp. 1703–1708, 2006.

[30] A. d'Entremont and A. Pilon, "First-order thermal model of commercial edlcs", *Applied Thermal Engineering*, vol. 67, no. 1, pp. 439–446, 2014.

[31] A. dEntremont and L. Pilon, "Scaling laws for heat generation and temperature oscillations in edlcs under galvanostatic cycling", *International Journal of Heat and Mass Transfer*, vol. 75, pp. 637–649, 2014.

[32] J. P. Sullivan, T. A. Friedman, and K. Hjort, "Diamond and amorphous carbon MEMS", *MRS Bulletin*, vol. 26, pp. 309–311, 2001.

[33] J. K. Luo, Y. Q. Fu, H. R. Le, J. A. Williams, S. M. Spearing, and W. I. Milne, "Diamond and diamond–like carbon MEMS", *Journal of Micromechanics and Microengineering*, vol. 17, pp. S147–S163, 2007.

[34] Rusli, S. F. Yoon, and Q. F. Huang, *Theory of Electric Polarization*, Elsevier Science Publishers, Amsterdam, The Netherlands, 1952.

[35] R. W. Zimmerman, "Thermal conductivity of fluid-saturated rocks", *Journal of Petroleum Science and Engineering*, vol. 3, no. 3, pp. 219 – 227, 1989.

[36] J. C. Maxwell Garnett, "Colours in metal glasses, in metallic films, and in metallic solutions. ii", *Philosophical Transactions of the Royal Society of London. Series A*, pp. 385–420, 1904.

[37] R. Landauer, "The electrical resistance of binary metallic mixtures", *Journal of Applied Physics*, vol. 23, no. 7, pp. 779–784, 1952.

[38] H. Looyenga, "Dielectric constants of heterogeneous mixtures", *Physica*, vol. 31, no. 3, pp. 401–406, 1965.

[39] S. R. P. Silva, *Properties of Amorphous Carbon*, vol. 29, EMIS Datareviews Series, Stevenage, UK, 2002.

[40] C. Casiraghi, A. C. Ferrari, and J. Robertson, "Raman spectroscopy of hydrogenated amorphous carbons", *Physical Review B*, vol. 72, pp. 085401, 2005.

[41] A. C. Ferrari, A. Libassi, B. K. Tanner, V. Stolojan, J. Yuan, L. M. Brown, S. E. Rodil, B. Kleinsorge, and J. Robertson, "Density, sp^3 fraction, and cross–sectional structure of amorphous carbon films determined by x–ray reflectivity and electron energy–loss spectroscopy", *Physical Review B*, vol. 62, pp. 11089–11103, 2000.

[42] F. Müller-Plathe, "A simple nonequilibrium molecular dynamics method for calculating the thermal conductivity", *The Journal of Chemical Physics*, vol. 106, no. 14, pp. 6082–6085, 1997.

[43] M. S. Green, "Markoff random processes and the statistical mechanics of time-dependent phenomena. II. Irreversible processes in fluids", *The Journal of Chemical Physics*, vol. 22, no. 3, pp. 398–413, 1954.

[44] R. Kubo, M. Yokota, and S. Nakajima, "Statistical-mechanical theory of irreversible processes. II. Response to thermal disturbance", *Journal of the Physical Society of Japan*, vol. 12, no. 11, pp. 1203–1211, 1957.

[45] P. Schelling, S. R. Phillpot, and P. Keblinski, "Comparison of atomic–level simulation methods for computing thermal conductivity", *Physical Review B*, vol. 65, pp. 144306, 2002.

[46] D. Frenkel and B. Smit, *Understanding Molecular Simulation From Algorithms to Applications*, Academic Press, San Diego, CA, 2nd edition, 2002.

[47] J. Fang and L. Pilon, "Tuning thermal conductivity of nanoporous crystalline silicon by surface passivation: A molecular dynamics study", *Applied Physics Letters*, vol. 101, no. 1, pp. 011909, 2012.

[48] J. Che, T. Cagin, W. Deng, and W. A. Goddard III, "Thermal conductivity of diamond and related materials from molecular dynamics simulations", *The Journal of Chemical Physics*, vol. 113, no. 16, pp. 6888–6900, 2000.

[49] J. Li, L. Porter, and S. Yip, "Atomistic modeling of finite–temperature properties of crystalline –SiC: II. Thermal conductivity and effects of point defects", *Journal of Nuclear Materials*, vol. 255, no. 2-3, pp. 139–152, 1998.

[50] J. Che, T. Çagin, and W. A. Goddard III, "Thermal conductivity of carbon nanotubes", *Nanotechnology*, vol. 11, no. 2, pp. 65, 2000.

[51] M. Joe, M.-W. Moon, and K.-R. Lee, "Atomistic simulations of diamond–like carbon growth", *Thin Solid Films*, vol. 521, pp. 239–244, 2012.

[52] J. Tersoff, "New empirical approach for the structure and energy of covalent systems", *Physical Review B*, vol. 37, pp. 6991–7000, 1988.

[53] N. A. Marks, "Generalizing the environment–dependent interaction potential for carbon", *Physical Review B*, vol. 63, pp. 035401, 2000.

[54] D. W. Brenner, "Empirical potential for hydrocarbons for use in simulating the chemical vapor deposition of diamond films", *Physical Review B*, vol. 42, pp. 9458–9471, 1990.

[55] D. W. Brenner, "Erratum: Empirical potential for hydrocarbons for use in simulating the chemical vapor deposition of diamond films", *Physical Review B*, vol. 46, pp. 1948–1948, 1992.

[56] J. Hu, S. Schiffli, A. Vallabhaneni, X. Ruan, and Y. P. Chen, "Tuning the thermal conductivity of graphene nanoribbons by edge passivation and isotope engineering: A molecular dynamics study", *Applied Physics Letters*, vol. 97, no. 13, pp. 133107, 2010.

[57] D. W. Brenner, O. A. Shenderova, J. A. Harrison, S. J. Stuart, B. Ni, and S. B. Sinnott, "A second–generation reactive empirical bond order (REBO) potential energy expression for hydrocarbons", *Journal of Physics: Condensed Matter*, vol. 14, pp. 7830802, 2002.

[58] S. J. Stuart, M. T. Knippenberg, O. Kum, and P. S. Krstic, "Simulation of amorphous carbon with a bond–order potential", *Physica Scripta*, vol. T124, pp. 58–64, 2006.

[59] D. G. Cahill and R. O. Pohl, "Heat flow and lattice vibrations in glasses", *Solid State Communications*, vol. 70, no. 10, pp. 927–930, 1989.

[60] D. G. Cahill, S. K. Watson, and R. O. Pohl, "Lower limit to the thermal conductivity of disordered crystals", *Physical Review B*, vol. 46, pp. 6131–6140, 1992.

[61] C. Mathioudakis, G. Kopidakis, P. C. Kelires, C. Z. Wang, and K. M. Ho, "Physical trends in amorphous carbon: A tight–binding molecular–dynamics study", *Physical Review B*, vol. 70, pp. 125202, 2004.

[62] S.-K. Chien, Y.-T. Yang, and C.-K. Chen, "Influence of hydrogen functionalization on thermal conductivity of graphene: Nonequilibrium molecular dynamics simulations", *Applied Physics Letters*, vol. 98, no. 3, pp. 033107, 2011.

[63] H.-C. Tsai and D. B. Bogy, "Characterization of diamondlike carbon films and their application as overcoats on thin–film media for magnetic recording", *Journal of Vacuum Science and Technology A*, vol. 5, no. 6, pp. 3287–3312, 1987.

[64] J. J. Cuomo, J. P. Doyle, J. Bruley, and J. C. Liu, "Sputter deposition of dense diamond–like carbon films at low temperature", *Applied Physics Letters*, vol. 58, no. 6, pp. 466–468, 1990.

[65] J. W. Zou, K. Schmidt, K. Reichelt, and B. Dischler, "The properties of a–C:H films deposited by plasma decomposition of C_2H_2", *Journal of Applied Physics*, vol. 67, no. 1, pp. 487–494, 1990.

[66] J. Li, X. Wang, Q. Huang, S. Gamboa, and P. J. Sebastian, "Studies on preparation and performances of carbon aerogel electrodes for the application of supercapacitor", *Journal of Power Sources*, vol. 158, no. 1, pp. 784–788, 2006.

[67] M. Wiener, G. Reichenauer, F. Hemberger, and H. P. Ebert, "Thermal conductivity of carbon aerogels as a function of pyrolysis temperature", *International Journal of Thermophysics*, vol. 27, no. 6, pp. 1826–1843, 2006.

[68] J. Feng, J. Feng, and C. Zhang, "Thermal conductivity of low density carbon aerogels", *Journal of Porous Materials*, vol. 19, pp. 551–556, 2012.

[69] S. Whitaker, *The Method of Volume Averaging*, vol. 13, Kluwer Academic Publisher, Dordrecht, The Netherlands, 1999.

[70] D. A. G. Bruggeman, "Berechnung verschiedener physikalischer konstanten von heterogenen substanzen. i. dielektrizittskonstanten und leitfhigkeiten der mischkrper aus isotropen substanzen", *Annalen der Physik*, vol. 416, no. 7, pp. 636–664, 1935.

[71] X. Lu, M. C. Arduini-Schuster, J. Kuhn, O. Nilsson, J. Fricke, and R. W. Pekala, "Thermal conductivity of monolithic organic aerogels", *Science*, vol. 255, no. 5047, pp. 971–972, 1992.

[72] M. Wang and N. Pan, "Predictions of effective physical properties of complex multiphase materials", *Materials Science and Engineering: R: Reports*, vol. 63, no. 1, pp. 1–30, 2008.

[73] R. L. Hamilton and O. K. Crosser, "Thermal conductivity of heterogeneous two–component systems", *Industrial & Engineering Chemistry Fundamentals*, vol. 1, no. 3, pp. 187–191, 1962.

[74] D. G. Cahill, "Heat transport in dielectric thin films and at solid-solid interfaces", *Microscale Thermophysical Engineering*, vol. 1, no. 2, pp. 85–109, 1997.

[75] G. Gesele, J. Linsmeier, V. Drach, J. Fricke, and R. Arens-Fischer, "Temperature-dependent thermal conductivity of porous silicon", *Journal of Physics D: Applied Physics*, vol. 30, no. 21, pp. 2911, 1997.

[76] A. Wolf and R. Brendel, "Thermal conductivity of sintered porous silicon films", *Thin Solid Films*, vol. 513, no. 1, pp. 385–390, 2006.

[77] S. J. Plimpton, "Fast parallel algorithms for short–range molecular dynamics", *Journal of Computational Physics*, vol. 117, no. 1, pp. 1–19, 1995.

[78] S. Nosé, "A unified formulation of the constant temperature molecular dynamics methods", *The Journal of Chemical Physics*, vol. 81, no. 1, pp. 511–519, 1984.

[79] W. G. Hoover, "Canonical dynamics: Equilibrium phase–space distributions", *Physical Review A*, vol. 31, pp. 1695–1697, 1985.

[80] M. E. Tuckerman, J. Alejandre, R. Lopez-Rendon, A. L. Jochim, and G. J. Martyna, "A Liouville–operator derived measure–preserving integrator for molecular dynamics simulations in the isothermal–isobaric ensemble", *Journal of Physics A*, vol. 39, pp. 5629–5651, 2006.

[81] F. H. Allen, O. Kennard, D. G. Watson, L. Brammer, A. G. Orpen, and R. Taylor, "Tables of bond lengths determined by X-ray and neutron diffraction. Part I. Bond lengths in organic compounds", *Journal of Chemical Society: Perkins Transactions II*, pp. S1–S19, 1987.

[82] J. M. Dickey and A. Paskin, "Computer simulation of the lattice dynamics of solids", *Physical Review*, vol. 188, pp. 1407–1418, 1969.

[83] J. L. Yarnell, M. J. Katz, R. G. Wenzel, and S. H. Koenig, "Structure factor and radial distribution function for liquid argon at 85 K", *Physical Review A*, vol. 7, pp. 2130–2144, 1973.

[84] A. S. Posner and F. Betts, "Synthetic amorphous calcium phosphate and its relation to bone mineral structure", *Bone Mineral Structure*, vol. 8, pp. 273–281, 1975.

[85] M. T. Knippenberg, *The Interaction Between Hydrogen and Various Carbon Allotropes Calculated Using Bond–Order Potentials*, PhD thesis, Clemson University, 2006.

[86] B. N. Jariwala, C. V. Ciobanu, and S. Agarwal, "Atomic hydrogen interactions with amorphous carbon thin films", *Journal of Applied Physics*, vol. 106, no. 7, pp. 073305, 2009.